PHYSICAL REVIEW E VOLUME 48, NUMBER 4 OCTOBER 1993

Paraxial wave-optics simulation of x-ray lasers

James W. Greene
Computational Physics Division, Lawrence Livermore National Laboratory, Livermore, California 94550

(Received 19 January 1993)

Paraxial wave-optics models of x-ray lasers include diffraction, time dependence, a stochastic description of spontaneous emission, two-way waves coupled by a saturable nonuniform gain, and refraction due to a nonuniform charge density. Standard algorithms for this modeling tax the speed and storage of a supercomputer. Recent work, using such algorithms on an overly coarse grid, has very distorted near fields, too wide far fields, and an optimistic estimation of spatial coherence. This paper develops axial shooting-secant iterations that feature coarse-grid storage of fields, refined-axial-step standard-algorithm shooting between coarse-grid data, and improved coarse-grid approximations via secant estimation. Such calculations, effective when the charge density and gain vary much more transversely than axially, save time and much storage. High-accuracy integral Hermitian methods for the transverse discretization are also introduced and provide several advantages in comparisions with standard finite differences, discrete Fourier transforms, and Gauss-Hermite or Gauss-Laguerre expansions. Several well-converged x-ray-laser calculations are presented. A slightly greater gain along certain curved paths contributes much less than refraction to prominent maxima in the far-field wings. Discrete computation inherently underestimates diffraction and thereby overestimates power output. Refraction enhances the evolution of single-mode-like intensity whereas saturation of the gain inhibits this process. The fields are sensitive to the transverse profiles of the charge density and small-signal gain. Although refraction leads to many more transverse modes, it improves spatial coherence.

PACS number(s): 02.60.−x, 02.70.−c, 42.25.−p, 42.55.Vc

I. INTRODUCTION

Research on x-ray lasers is burgeoning worldwide and should lead to a broad array of important applications [1,2]. These lasers involve an intricate mix of atomic kinetics, hydrodynamics, and optics. Relatively simple analytical and numerical modeling, using geometric optics and having only an unsaturable gain, gives quite a bit of insight [3]. However, an assessment of coherence, saturable gain, and diffractive effects is also needed and demands a wave-optics treatment, the difficulty of which requires extensive numerical simulation. Such computation may help with the optimization of x-ray lasers, which is important because their best possible performance may be only moderate, or even marginal.

Feit and Fleck [4] offer a complex description based on paraxial wave optics. Garrison *et al.* [5] provide much more detailed modeling—macroscopic and microscopic. They even include a transverse paraxial pumping wave, but their calculations treat a dye laser, which requires less computational power than the x-ray calculations undertaken by Feit and Fleck.

These papers do not treat hydrodynamics or really intricate atomic kinetics. Such calculations for x rays are precluded because the two-way advective-marching algorithms of paraxial wave optics are so demanding that they can, just by themselves, tax or overwhelm the most powerful computers. This circumstance insidiously encourages using too few points in order to reduce the computing burden. For example, calculations below ascertain that an overly sparse grid used by Feit and Fleck [4] needs at least five times more points to yield only modest convergence. Using their algorithms on such a more refined grid severely taxes the capacity of a Cray-Y/MP8.

This paper focuses upon reducing the computational burden of the two-way advective-marching algorithms via more efficient, iterative strategies with these algorithms. High-accuracy transverse discretization, derived from integral Hermitian methods, is also introduced and compared with standard finite differences, discrete Fourier transforms, and Gauss-Hermite or Gauss-Laguerre expansions. A variety of calculations relevant to the modeling of x-ray lasers is included. Like preceding work [3,4], the computations deal only with simple time-independent profiles of the charge density and small-signal gain. There is no coupling to hydrodynamics or detailed atomic kinetics. No microscopic analyses are considered—simple macroscopic models of gain, refraction, and spontaneous-emission sources suffice to demonstrate the effectiveness of the computational methods. The more efficient algorithms provide well-converged simulations of the macroscopic optics and still save time and much storage, which can be used for hydrodynamics and elaborate atomic kinetics.

Section II outlines various physical assumptions and the basic paraxial wave-optics equations. Section III is subdivided in the following way: Sec. III A casts the paraxial wave-optics equations in terms of the geometric theory for first-order quasilinear partial differential equations [6], which helps, I think, to visualize the subsequent iterative algorithms; Sec. III B describes axial discretization for time-independent, time-dependent, one-way, and two-way transport—shorting-secant iterations appear in the analysis of two-way transport; Sec. III C compares

1063-651X/93/48(4)/3130(31)/$06.00

various methods for the transverse discretization—Fourier transforms, Gauss-Hermite or Gauss-Laguerre expansions, standard finite differences, and finite differences derived from an integral Hermitian approach; Sec. III D discusses models of the charge density and the gain, the spontaneous emission in terms of random-walk linear-gain relations, and the transverse coherence calculations. The calculations in Sec. IV illustrate the preceding analyses and display various properties of the x-ray output—Sec. IV A deals mainly with relatively inexpensive one-way computation while much more expensive two-way calculations appear in Sec. IV B. Section V has concluding remarks and suggests some directions for further work.

II. PARAXIAL WAVE-OPTICS MODELING OF X-RAY LASERS

The macroscopic field in an x-ray laser arises from the amplification of spontaneous emission in a very slender plasma. Figure 1 depicts a typical configuration of the laser. Its "axis" coincides with the z axis. Henceforth the words "axial" and "transverse" refer, respectively, to this z axis and any direction perpendicular to it.

An interplay of diffraction, refraction, saturable gain, spontaneous emission, hydrodynamics, and atomic kinetics determines the macroscopic output of the laser. Spontaneous emission generates a tremendous number of "modes." Diffraction spreads the radiation, and the amount of spreading increases with the mode index. The charge density and small-signal gain of the plasma, which are dynamic because of hydrodynamic expansion and atomic kinetics, have the following spatial properties: (a) they are large near the z axis and vanish outside the near-axis region; (b) their transverse variation is much greater than their axial variation. Consequently, refraction, which bends rays toward lower concentrations of charge, also spreads the radiation. Since diffraction and refraction spread the radiation into regions with less gain, they reduce the overall amplification. The field becomes large enough to saturate the small-signal gain. Since the gain is greater near the z axis, it saturates there before it does so in the transverse wings of the plasma. This differential saturation can therefore flatten the transverse distribution of the field. The spontaneous emission also generates two-way waves, which are coupled via their respective contributions to the saturation. Despite the various factors that spread the radiation in the laser, its axial length is so long in relation to its transverse size that most of its relevant output is channeled into narrow pencils of rays at its ends. It is therefore possible to describe this output with paraxial waves.

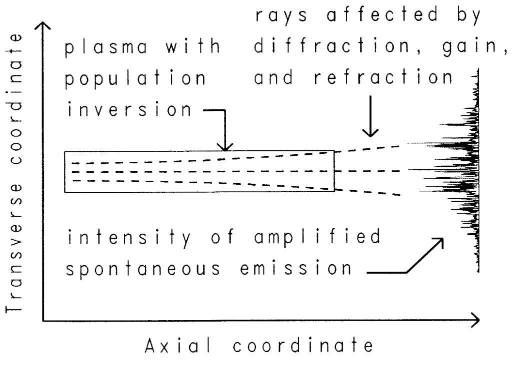

FIG. 1. A schematic of an amplifier of spontaneous x-ray emission. A typical computed output is displayed. The transverse dimension of the drawing is greatly exaggerated.

Many projected applications of x-ray lasers, e.g., the holography of biological specimens, require a sufficiently high degree of spatial and temporal coherence [7], the analysis of which requires information about the amplitude and phase and hence necessitates a wave treatment. Because x-ray mirrors are relatively inefficient, relatively poor mode selection and modest coherence may always result. The laser is likely to remain a many-mode device operating far from a steady state. Moreover, only a few passes through the laser are attainable before the gain subsides. Time dependence is therefore an essential feature of the laser.

A paraxial wave-optics analysis of x-ray lasers inherently describes diffraction. In summary, such an analysis must also include time dependence, spontaneous emission, two-way waves coupled by a saturable nonuniform gain, and refraction due to a nonuniform density of charge. Furthermore, incorporating detailed atomic kinetics and hydrodynamics into the analysis would be highly desirable for accurate modeling.

To characterize the dielectric constant ϵ of the plasma, let me use the relatively simple high-frequency formula [8]

$$\epsilon=\epsilon_0-\frac{4\pi n_e e^2}{m_e\omega^2}\ , \tag{1}$$

where n_e, e, m_e, and ω are, respectively, the free-electron number density, the electron charge, the electron mass, and the x-ray angular frequency. The following modeling does not preclude a more detailed description of the plasma's dielectric properties, but this simple formula suffices for what I want to discuss.

In order to set up a paraxial approximation, define a suitable space-time average for the dielectric constant, i.e.,

$$\epsilon_a=\langle\epsilon\rangle_{x,y,z,t}\ . \tag{2}$$

Then a two-way plane-polarized monochromatic field can be represented in the form of plane waves having "slowly varying" amplitudes $E^{\pm}$, angular frequency ω, and wave number $\omega c^{-1}\sqrt{\epsilon_a}$ (c is the velocity of light in vacuum):

$$E(x,y,z,t)=E^{+}(x,y,z,t)\exp[i\omega(c^{-1}\sqrt{\epsilon_a}z-t)]+E^{-}(x,y,z,t)\exp[-i\omega(c^{-1}\sqrt{\epsilon_a}z+t)]\ . \tag{3}$$

Substitute this expression into the wave equation

$$\nabla^2E=\frac{\epsilon}{c^2}\frac{\partial^2E}{\partial t^2}\ ; \tag{4}$$

specify that $E^{\pm}$ are "slowly varying" in the sense of the inequalities

$$\left|\frac{\partial^2 E^\pm}{\partial z^2}\right| \ll \frac{\omega^2\epsilon_a}{c^2}|E^\pm|, \quad \left|\frac{\partial^2 E^\pm}{\partial t^2}\right| \ll \omega^2|E^\pm| \; ; \tag{5}$$

and then neglect $\partial^2 E^\pm/\partial z^2$ and $\partial^2 E^\pm/\partial t^2$ in comparison to the much larger terms indicated by these inequalities. One thereby obtains

$$\frac{\partial E^\pm}{\partial z} \pm \frac{\epsilon}{c\sqrt{\epsilon_a}}\frac{\partial E^\pm}{\partial t} = \pm i\frac{c}{2\omega\sqrt{\epsilon_a}}\nabla_\perp^2 E^\pm \pm i\frac{\omega}{2c\sqrt{\epsilon_a}}(\epsilon-\epsilon_a)E^\pm \; , \tag{6}$$

where the transverse Laplacian

$$\nabla_\perp^2 = \nabla^2 - \frac{\partial^2}{\partial z^2} \; . \tag{7}$$

Equations (6) describe the combined effects of diffraction and refraction. It is customary to neglect the small transverse variations of velocity in the advective terms of Eqs. (6), i.e.,

$$\frac{\epsilon}{\sqrt{\epsilon_a}} \approx \sqrt{\epsilon_a} \; . \tag{8}$$

One can also arrive at the same results more rigorously by beginning with the first-order Maxwell equations [9]. Such an approach requires additional assumptions about the smallness of various terms involving $E^\pm$, ϵ, and their spatial and time derivatives.

A macroscopic description of saturable nonuniform gain is provided by the oft-used gain coefficient [10]

$$g = \frac{g_0(x,y,z,t)}{1+(|E^+|^2+|E^-|^2)/I_{\text{sat}}} \; , \tag{9}$$

in which (a) g_0 is a nonuniform small-signal gain; (b) two-way waves are coupled as if they arise from statistically independent sources [i.e., the sum $(|E^+|^2+|E^-|^2)$ adds the intensities without interference whereas a squared sum like $|E^+ + E^-|^2$ has interference terms]; and (c) the parameter I_{sat} equals the two-way intensity at which the gain is saturated down to one-half of its small-signal value. Of course, the two-way waves should be statistically independent because they are generated by spontaneous emission.

Limitations in storage and speed preclude a computer simulation of spontaneous emission at a microscopic level. The intensity of spontaneous emission ought to vary smoothly with respect to a macroscopic resolution. On the other hand, the phases of this radiation should be uncorrelated down to the smallest scale that can be simulated by a computer. Therefore, consider the following macroscopic representation of the two-way spontaneous emission:

$$S^\pm(x,y,z,t) = A^\pm(x,y,z,t)\exp[i\Phi^\pm(x,y,z,t)] \; , \tag{10}$$

where $A^\pm$ are taken to be definite functions that vary relatively smoothly while $\Phi^\pm$ are described stochastically and vary much more rapidly. In this way, the intensity $|S^\pm|^2$ of the spontaneous emission varies smoothly while its phase variation can be arbitrarily complex.

Let me define the scaled variables

$$\mathcal{E}^\pm = \frac{E^\pm}{\sqrt{I_{\text{sat}}}}, \quad \mathcal{S}^\pm = \frac{S^\pm}{\sqrt{I_{\text{sat}}}} \; . \tag{11}$$

Then, Eqs. (6) and (8)–(10) lead to

$$\frac{\partial \mathcal{E}^\pm}{\partial z} \pm \frac{\sqrt{\epsilon_a}}{c}\frac{\partial \mathcal{E}^\pm}{\partial t} = \pm i\frac{c}{2\omega\sqrt{\epsilon_a}}\nabla_\perp^2\mathcal{E}^\pm \pm i\frac{\omega}{2c\sqrt{\epsilon_a}}(\epsilon-\epsilon_a)\mathcal{E}^\pm \pm \frac{g}{2}\mathcal{E}^\pm + \mathcal{S}^\pm \; , \tag{12}$$

where $g = g_0/(1+|\mathcal{E}^+|^2+|\mathcal{E}^-|^2)$. The gain coefficient g in Eqs. (12) is divided by 2 so that the intensities $|\mathcal{E}^\pm|^2$ rather than the fields $\mathcal{E}^\pm$ behave like $\exp(gz)$. The transverse boundary conditions for Eqs. (12) may be taken to be

$$\lim_{x,y\to\infty} \mathcal{E}^\pm(x,y,z,t) = \lim_{x,y\to\infty} \nabla_\perp \mathcal{E}^\pm(x,y,z,t) = 0 \; . \tag{13}$$

Any external radiation entering the ends of the laser can obviously be specified by axial boundary conditions. In the absence of such radiation, the laser's fields evolve solely from the spontaneous-emission sources $\mathcal{S}^\pm$ in Eqs. (12).

III. COMPUTATIONAL METHODS

A. Kinematics and dynamics

Despite the presence of the transverse Laplacian, it is possible, and useful, to interpret Eqs. (12) with the geometric theory for first-order quasilinear partial differential equations [6]. The structure of Eqs. (12) suggests the generalized characteristic differential equations

$$\frac{dx}{ds^\pm}=0, \quad \frac{dy}{ds^\pm}=0, \quad \frac{dz}{ds^\pm}=1, \quad \frac{dt}{ds^\pm}=\pm\frac{\sqrt{\epsilon_a}}{c} \; , \tag{14}$$

$$\frac{d\mathcal{E}^\pm}{ds^\pm} = \pm i\frac{c}{2\omega\sqrt{\epsilon_a}}\nabla_\perp^2\mathcal{E}^\pm \pm i\frac{\omega}{2c\sqrt{\epsilon_a}}(\epsilon-\epsilon_a)\mathcal{E}^\pm \pm \frac{g}{2}\mathcal{E}^\pm + \mathcal{S}^\pm \; , \tag{15}$$

where the parameters $s^\pm$ measure arclength in the forward or backward directions along the characteristic curves. The advective velocity $c/\sqrt{\epsilon_a}$ is constant. Equations (14) therefore imply that (a) the projection of each characteristic curve onto xyz space (i.e., an "xyz-projected characteristic base curve") is a line parallel to the z axis, and (b) a time increment δt corresponds to the same spatial increment δz on every such characteristic base line. The transverse Laplacian terms in Eqs. (15) indicate also that the base-line evolution of $\mathcal{E}^\pm$ is affected by their values on neighboring base lines. In other words, each transverse section of field points (x,y) remains planar and advects parallel to the z axis with a constant velocity while the corresponding field values $\mathcal{E}^\pm(x,y,z,t)$ evolve concurrently in accordance with Eqs. (15). This geometric picture of the advection would be more complicated if the approximation of Eq. (8) were not in effect.

While keeping the xy variations continuous, one can discretize the zt variations of the fields $\mathcal{E}^{\pm}$ onto a set of transverse sections separated by a uniform axial increment δz. As the fields advance through the spatial step δz, they evolve temporally through the increment δt, where $\delta t = \sqrt{\epsilon_a}\,\delta z / c$. If the assembly of transverse sections is regarded to be fixed with respect to the laser, the field points advect along the intersections of the characteristic base lines with the transverse sections. The forward-field points move in the positive z direction while the backward-field points move oppositely. If an xy discretization is added to the foregoing zt discretization, the continuous density of projected characteristic base lines is replaced by a discrete set of these lines. The space-time evolution of the associated field values $\mathcal{E}^{\pm}$ is thus recorded on a laser-fixed assembly of transverse sections.

A kinematic alternative, which is particularly convenient in the case of one-way propagation [e.g., $\mathcal{E}^{-} = \mathcal{S}^{-} = 0$ in Eqs. (12)], moves the assembly of transverse sections axially at the velocity $c/\sqrt{\epsilon_a}$, i.e., the assembly is fixed with respect to the moving beam pulse $\mathcal{E}^{+}$. In such a uniformly moving coordinate system, each field point is fixed inside a particular transverse section as the corresponding field value evolves via the forward member of Eqs. (15).

If the free-electron density, gain, and sources are steady ($\partial\epsilon/\partial t = \partial g/\partial t = \partial\mathcal{S}^{\pm}/\partial t = 0$), every solution of Eqs. (14) and (15) evolves transiently into a steady state ($\partial\mathcal{E}^{\pm}/\partial t = 0$). For a steady state, Eqs. (14) can be simplified to

$$\frac{dx}{ds^{\pm}} = 0, \quad \frac{dy}{ds^{\pm}} = 0, \quad \frac{dz}{ds^{\pm}} = 1 , \tag{16}$$

so that unprojected characteristic base curves are lines parallel to the z axis. Of course, the forms of Eqs. (15) do not change for a steady state, which is merely a special solution of them. The aforementioned laser-fixed assembly of transverse sections is also convenient for an xyz discretization of both one-way and two-way steady-state problems.

If only the gain and free-electron density are steady ($\partial g/\partial t = \partial\epsilon/\partial t = 0$), any initial fields evolve transiently into a near steady state ($\partial\mathcal{E}^{\pm}/\partial t \approx 0$) in which the fields are changing only slightly in response to the fluctuating sources. A simulation of this near steady state can be obtained from a full time-dependent analysis with Eqs. (14) and (15). One may alternatively deal with time-independent sources ($\partial\mathcal{S}^{\pm}/\partial t = 0$) by regarding each stochastic realization of the sources as a member of an ensemble of steady-state sources. For each member of this ensemble, there is an exact steady state ($\partial\mathcal{E}^{\pm}/\partial t = 0$) described by Eqs. (15) and (16). Small fluctuations of the fields, i.e., the near steady states, are then represented by a sequence of steady-state solutions corresponding to steady-state sources taken from the ensemble. Even though the time-dependent approach involves transients not present in the steady-state analysis, there is probably little practical difference in the results of these two approaches. However, the numerical procedures required by these approaches are quite different.

Equations (15) may be regarded as an xy-continuous system of two-way-coupled nonlinear first-order differential equations with sources. They can be solved, in conjunction with Eqs. (14), when one specifies initial values, the transverse boundary conditions [Eqs. (13)], and any axial boundary conditions arising from external radiation. Similarly, Eqs. (13), (15), and (16) have steady-state solutions when the density, gain, sources, and external radiation are steady.

B. Axial discretization

1. One-way time-independent transport

Let the xy variation be continuous and implicit in the notation and consider the simplest propagation—no sources, one-way transport, and no time dependence. Then, if $\mathcal{E}^{-} = \mathcal{S}^{\pm} = 0$ and $\mathcal{F} = \mathcal{E}^{+}$, Eqs. (15) reduce to the form

$$\frac{d\mathcal{F}}{dz} = \alpha\nabla_{\perp}^{2}\mathcal{F} + \beta(z,\mathcal{F})\mathcal{F} , \tag{17}$$

whose solution may be expressed implicitly

$$\mathcal{F}(z) = \mathcal{F}(0) + \int_0^z [\alpha\nabla_{\perp}^2 + \beta(\mu,\mathcal{F}(\mu))]\mathcal{F}(\mu)\,d\mu . \tag{18}$$

Setting $a(\mu) = \alpha\nabla_{\perp}^2 + \beta(\mu,\mathcal{F}(\mu))$, and iterating Eq. (18) as a transversely continuous Neumann series [11], one obtains

$$\begin{aligned}\mathcal{F}(z) &= \mathcal{F}(0) + \int_0^z a(\mu)\left[\mathcal{F}(0) + \int_0^\mu a(\nu)\mathcal{F}(\nu)\,d\nu\right]d\mu \\ &= \left[1 + \int_0^z a(\mu)\,d\mu + \int_0^z a(\mu)\,d\mu\int_0^\mu a(\nu)\,d\nu + \int_0^z a(\mu)\,d\mu\int_0^\mu a(\nu)\,d\nu\int_0^\nu a(\xi)\,d\xi + \cdots\right]\mathcal{F}(0) \\ &\equiv \exp\left[\int_0^z a(\mu)\,d\mu\right]\mathcal{F}(0) .\end{aligned} \tag{19}$$

Fleck, Morris, and Feit [12] show that

$$\exp\left[\int_0^z a(\mu)\,d\mu\right] = \exp(\tfrac{1}{2}\alpha\nabla_{\perp}^2 z)\exp\left[\int_0^z \beta(\mu,\mathcal{F}(\mu))\,d\mu\right] \times \exp(\tfrac{1}{2}\alpha\nabla_{\perp}^2 z) + O(z^3) , \tag{20}$$

when $\beta(z,\mathcal{F}(\mu))$ can be represented by a power series in z.

Similar considerations establish an alternative splitting of the exponential operators:

$$\exp\left[\int_0^z a(\mu)\,d\mu\right] = \exp\left[\tfrac{1}{2}\int_0^z \beta(\mu,\mathcal{F}(\mu))\,d\mu\right]\exp(\alpha\nabla_{\perp}^2 z) \times \exp\left[\tfrac{1}{2}\int_0^z \beta(\mu,\mathcal{F}(\mu))\,d\mu\right] + O(z^3) . \tag{21}$$

Consequently, Eqs. (17), (19), and (21) imply that

$$\mathcal{F}(z)=\exp\left[\tfrac{1}{2}\int_0^z \beta(\mu,\mathcal{F}(\mu))d\mu\right]\exp(\alpha\nabla_\perp^2 z)\times\exp\left[\tfrac{1}{2}\int_0^z \beta(\mu,\mathcal{F}(\mu))d\mu\right]\mathcal{F}(0)+O(z^3)\ . \tag{22}$$

The computational implementation of Eq. (22) is straightforward. Let a field $\mathcal{F}(0)$ be defined over any one of the transverse planes described in Sec. III A. Then, compute and store the elements of the "xy-diagonal" operator $\exp[\frac{1}{2}\int_0^z \beta(\mu,\mathcal{F}(\mu))d\mu]$. For example, the trapezoidal rule gives the following amplitude-phase multiplier for the axial interval $(0,z)$:

$$\begin{aligned}M(0,z)&=\exp\{\tfrac{1}{4}[\beta(0,\mathcal{F}(0))+\beta(z,\mathcal{F}(z))]z+O(z^3)\}\\&\approx\exp\{\tfrac{1}{4}[\beta(0,\mathcal{F}(0))+\beta(z,\mathcal{F}(0))]z\}\ ,\end{aligned} \tag{23}$$

the first approximate form of which has a truncation error consistent with Eq. (22) and the second approximate form of which is needed to obtain an algorithm explicit in $\mathcal{F}(0)$. The alternative splitting in Eq. (20) requires the same phase approximation. The output $M(0,z)\mathcal{F}(0)$ becomes the source for the vacuum operator $\exp(\alpha\nabla_\perp^2 z)$, whose discretization is discussed in Sec. III C. Finally, an $M(0,z)$ multiplication of the vacuum-operator output $\exp(\alpha\nabla_\perp^2 z)M(0,z)\mathcal{F}(0)$ yields the approximate field $\mathcal{F}(z)$, viz.,

$$\mathcal{F}(z)\approx M(0,z)\exp(\alpha\nabla_\perp^2 z)M(0,z)\mathcal{F}(0)\ . \tag{24}$$

Notice that $\mathcal{F}(z)$ is a steady-state solution. The axial variable z need not be greater than 0 so backward as well as forward "marching" of the steady-state solution is possible. The steady-state field has to be specified on only one transverse plane in order to determine its values over any other such plane by repeatedly applying Eq. (24) with sufficiently small axial steps. Moreover, the field is stored on only one transverse plane throughout such a computation.

The evaluation of the exponentials in Eq. (23) entails much more computing time than the two multiplications by $M(0,z)$ in Eq. (24). It is therefore important to save $M(0,z)$ after its evaluation so that it does not have to be recomputed for the second multiplication in Eq. (24).

A repeated application of Eq. (24) juxtaposes amplitude-phase multipliers of the form $M[nz,(n+1)z]$ so one might be tempted to combine juxtaposed exponentials into a single exponential for a doubled axial step. However, such a combination is not strictly correct since

$$\begin{aligned}M(z,2z)M(0,z)&=\exp\{\tfrac{1}{4}[\beta(z,\mathcal{F}(z))+\beta(2z,\mathcal{F}(z))]z\}\\&\quad\times\exp\{\tfrac{1}{4}[\beta(0,\mathcal{F}(0))+\beta(z,\mathcal{F}(0))]z\}\\&\neq\exp\{\tfrac{1}{4}[\beta(0,\mathcal{F}(0))+\beta(2z,\mathcal{F}(0))]2z\}\\&=M(0,2z)\ .\end{aligned} \tag{25}$$

The factor $\exp(\frac{1}{2}\alpha\nabla_\perp^2 z)$ in Eq. (20) can be combined under juxtaposition. The splitting in Eq. (20) may therefore seem to be preferable, but, as long as the amplitude-phase multiplier $M(0,z)$ is saved for the second multiplication in Eq. (24), this apparent advantage of Eq. (20) is inconsequential. It is sometimes claimed that the operator splitting in Eq. (20) is superior. Numerical testing yields, at least for the applications considered herein, virtually identical results for the splitting in Eq. (21), which is used for the calculations in Sec. IV.

If a one-way steady-state axially distributed source $\mathcal{S}(z)$ is present, Eq. (17) generalizes to the form

$$\frac{d\mathcal{F}}{dz}=\alpha\nabla_\perp^2\mathcal{F}+\beta(z,\mathcal{F})\mathcal{F}+\mathcal{S}\ , \tag{26}$$

so

$$\begin{aligned}\mathcal{F}(z)&=\mathcal{F}(0)+\int_0^z\{[\alpha\nabla_\perp^2+\beta(\mu,\mathcal{F}(\mu))]\mathcal{F}(\mu)+\mathcal{S}(\mu)\}d\mu\\&=\mathcal{F}(0)+\tfrac{1}{2}[\mathcal{S}(0)+\mathcal{S}(z)]z\\&\quad+\int_0^z[\alpha\nabla_\perp^2+\beta(\mu,\mathcal{F}(\mu))]\mathcal{F}(\mu)d\mu+O(z^3)\end{aligned} \tag{27}$$

by virtue of the trapezoidal rule. Although the preceding Neumann-series analysis of Eq. (18) could be repeated with this more general expression, such complexity is not justified for stochastic sources. It suffices instead to generate a stochastic increment $\mathcal{S}$ of appropriate amplitude and random phase and to add it to the field at the beginning of each axial step. Equation (24) thereby becomes

$$\mathcal{F}(z)\approx M(0,z)\exp(\alpha\nabla_\perp^2 z)M(0,z)[\mathcal{F}(0)+\mathcal{S}]\ . \tag{28}$$

2. One-way time-dependent transport

A further generalization to time-dependent one-way transport requires only the addition of advective time corrections to the marching algorithm given by Eq. (28). The time-dependent analogue of Eq. (26) is

$$\frac{d\mathcal{F}}{dz}=\alpha\nabla_\perp^2\mathcal{F}+\beta(t,z,\mathcal{F})\mathcal{F}+\mathcal{S}\ , \tag{29}$$

where the time dependences of the free-electron density and gain are represented explicitly. Equations (14) and (15) show that the spatial step of length z in Eq. (29) corresponds to the advective time step $t=\sqrt{\epsilon_a}z/c$. Therefore, the amplitude-phase multiplier in Eq. (23) generalizes to the time-dependent form

$$M(0,z)\approx\exp\{\tfrac{1}{4}[\beta(0,0,\mathcal{F}(0))+\beta(\sqrt{\epsilon_a}z/c,z,\mathcal{F}(0))]z\}\ , \tag{30}$$

while the form of Eq. (28) remains unchanged for time-dependent transport.

A typical calculation with only one transverse section might proceed in the following way. Starting at one end of the laser, one sets $\mathcal{F}(0)$ equal to the field of an input beam and then applies Eq. (28) recursively until the section advects axially and temporally to the other end of the laser. If such a calculation were repeated many times, always with the same input field, but each time with a different sequence of stochastically generated spontaneous-emission increments, one would obtain the output beam along with its statistical fluctuations.

Of course, the axial resolution of such a calculation can be increased by using more transverse sections. Because the requisite computing storage for each transverse section is so large, the total number of such sections is limited to much less than the number of axial steps needed to adequately resolve the diffraction, gain, and refraction. This circumstance—namely that the number of transverse sections can be much less than the number of axial steps in a time-dependent calculation—arises because the free-electron density and gain vary much more transversely than axially and evolve quasistatically, at least for a time required by light to transit the laser.

3. Two-way time-dependent transport

Two-way-coupled transport poses a much more difficult problem than one-way transport. Let $\mathcal{B}=\mathcal{E}^-$ and $\mathcal{F}=\mathcal{E}^+$. Equations (15) become

$$\frac{d\mathcal{B}}{dz}=-\alpha\nabla_\perp^2\mathcal{B}-\beta(t,z,\mathcal{B},\mathcal{F})\mathcal{B}+\mathcal{S}^- \ , \tag{31}$$

$$\frac{d\mathcal{F}}{dz}=\alpha\nabla_\perp^2\mathcal{F}+\beta(t,z,\mathcal{B},\mathcal{F})\mathcal{F}+\mathcal{S}^+ \ . \tag{32}$$

If the preceding analysis for one-way time-dependent transport is retraced, a backward integration of Eq. (31) and a forward integration of Eq. (32) yield the following analogs of Eq. (28):

$$\mathcal{B}(0)\approx N(0,z)\exp(\alpha\nabla_\perp^2 z)N(0,z)[\mathcal{B}(z)+\mathcal{S}^-(z)] \ , \tag{33}$$

$$\mathcal{F}(z)\approx N(0,z)\exp(\alpha\nabla_\perp^2 z)N(0,z)[\mathcal{F}(0)+\mathcal{S}^+(0)] \ , \tag{34}$$

where

$$N(0,z)\approx \exp\{\tfrac{1}{4}[\beta(0,0,\mathcal{B}(z),\mathcal{F}(0)) +\beta(\sqrt{\epsilon_a}z/c,z,\mathcal{B}(z),\mathcal{F}(0))]z\} \ . \tag{35}$$

If the interval $(0,z)$ is sufficiently small, Eqs. (33)–(35) permit, at least in principle, an accurate simulation over a laser-fixed assembly of transverse sections. Equation (33) adds a spontaneous-emission increment to the backward field $\mathcal{B}(z)$ and computes its backwardly advected output $\mathcal{B}(0)$ while Eq. (34) accomplishes the same thing for the forward field $\mathcal{F}(0)$. The backward and forward fields of the laser advance over one space-time step when this calculation is performed for each adjacent pair of transverse sections.

Feit and Fleck [4] essentially follow this "brute-force" approach—they use the alternative splitting of Eq. (20) and evaluate the operator $\exp(\frac{1}{2}\alpha\nabla_\perp^2 z)$ via discrete Fourier transformation. The computations in Sec. IV demonstrate that this procedure can outstrip the capacity of a supercomputer such as a CRAY-Y/MP8. The irony of this computational method is that the fields are stored at the density of the paraxial steps even though paraxial approximations are usually undertaken to avoid such a density of storage. This enormous storage and a considerable amount of computing time can, in fact, be circumvented by iterative generalizations based on Eqs. (33)–(35).

It is easy to construct such iterations. Let several of the small intervals $(0,z)$ associated with Eqs. (33)–(35) be linked together to form the interval

$$(0,Z)=(0,mz) \quad (m=1,2,\dots) \ . \tag{36}$$

Suppose further that the forward and backward fields and the spontaneous-emission increments are defined and stored only at the endpoints of the interval $(0,Z)$. If Eq. (33) is applied recursively,

$$\begin{aligned}\mathcal{B}(0)=&N(0,z)\exp(\alpha\nabla_\perp^2 z)N(0,z)N(z,2z)\exp(\alpha\nabla_\perp^2 z)N(z,2z)\cdots N(Z-z,Z)\exp(\alpha\nabla_\perp^2 z)N(Z-z,Z)\\&\times[\mathcal{B}(Z)+\mathcal{S}^-(Z)]=U(0,Z)[\mathcal{B}(Z)+\mathcal{S}^-(Z)] \ ,\end{aligned} \tag{37}$$

where

$$N(nz,nz+z)\approx \exp\{\tfrac{1}{4}[\beta(\sqrt{\epsilon_a}nz/c,nz,\mathcal{B}(nz+z),\mathcal{F}(nz))+\beta(\sqrt{\epsilon_a}(nz+z)/c,nz+z,\mathcal{B}(nz+z),\mathcal{F}(nz))]z\} \quad (n=0,1,\dots,m-1) \ , \tag{38}$$

and where the operator $U(0,Z)$ transports the backward field through the entire interval $(0,Z)$. Equations (35) and (37) imply that $U(0,Z)$ has the inverse

$$\begin{aligned}U^{-1}(0,Z)=&N^{-1}(Z-z,Z)\exp(-\alpha\nabla_\perp^2 z)N^{-1}(Z-z,Z)N^{-1}(Z-2z,Z-z)\exp(-\alpha\nabla_\perp^2 z)\\&\times N^{-1}(Z-2z,Z-z)\cdots N^{-1}(0,z)\exp(-\alpha\nabla_\perp^2 z)N^{-1}(0,z) \ ,\end{aligned} \tag{39}$$

where

$$N^{-1}(nz,nz+z)\approx \exp\{-\tfrac{1}{4}[\beta(\sqrt{\epsilon_a}nz/c,nz,\mathcal{B}(nz+z),\mathcal{F}(nz))+\beta(\sqrt{\epsilon_a}(nz+z)/c,nz+z,\mathcal{B}(nz+z),\mathcal{F}(nz))]z\} \quad (n=0,1,\dots,m-1) \ . \tag{40}$$

Therefore, Eq. (37) and the recursive application of Eq. (34) yield

$$\mathcal{B}(Z)=U^{-1}(0,Z)\mathcal{B}(0)-\mathcal{S}^-(Z) \ , \tag{41}$$

$$\mathcal{F}(Z)=U(0,Z)[\mathcal{F}(0)+\mathcal{S}^+(0)] \ . \tag{42}$$

The operator $U(0,Z)$ is built from a recursive algorithm in which a step-by-step tandem application of Eqs. (33) and (34) is required to determine the intermediate backward and forward fields. If an approximate field $\tilde{\mathcal{B}}(0)$ is guessed, Eqs. (41) and (42) permit one to calculate approximate fields $\tilde{\mathcal{B}}(Z)$ and $\tilde{\mathcal{F}}(Z)$ from $\tilde{\mathcal{B}}(0)$ and the known quantities $\mathcal{F}(0)$, $\mathcal{S}^+(0)$, and $\mathcal{S}^-(Z)$. Iterative improvements of $\tilde{\mathcal{B}}(0)$ and $\tilde{\mathcal{F}}(Z)$ can then be obtained by comparing the approximation $\tilde{\mathcal{B}}(Z)$ against the known field $\mathcal{B}(Z)$.

Equations (41) and (42) constitute a nonlinear functional transformation

$$\mathcal{B}(Z)=T[\mathcal{B}(0)] \tag{43}$$

defined by an elaborate advective-marching algorithm. A determination of the inverse transformation

$$\mathcal{B}(0)=T^{-1}[\mathcal{B}(Z)] \tag{44}$$

is needed and can be approximated in a number of ways. The procedure below employs "shooting" with Eq. (43) and iterative refinements based on "secant" interpolation.

Let ψ_i $(i=1,2,\ldots)$ denote a sequence of approximations to the field $\mathcal{B}(0)$ in Eq. (43), consider two successive approximations ψ_i and ψ_{i+1} that bracket $\mathcal{B}(0)$ in the manner depicted in Fig. 2, and pass a straight line through the points $(\psi_i, T(\psi_i))$ and $(\psi_{i+1}, T(\psi_{i+1}))$ to obtain an approximate functional $\tilde{T}(\psi)$. The improved approximation is taken to be $\psi_{i+2}=\tilde{T}^{-1}[\mathcal{B}(Z)]$, i.e., the successive approximations

$$\psi_{i+2}=\psi_{i+1}+\frac{\mathcal{B}(Z)-T(\psi_{i+1})}{T(\psi_i)-T(\psi_{i+1})}(\psi_i-\psi_{i+1}) \quad (i=1,2,\ldots) \tag{45}$$

are computed in a *scalar* fashion at each point of the transverse grid.

This sequence is fully defined when the first two approximations ψ_1 and ψ_2 are specified. The amount of computation needed to converge satisfactorily depends upon how accurately one chooses these quantities. The following technique works well for the computations in Sec. IV. First, set $\mathcal{B}(0)=0$ and use Eq. (42) to compute an approximation $\tilde{\mathcal{F}}(Z)$. Then, multiply $[\mathcal{B}(Z)+\mathcal{S}^-(Z)]$ by the complex factors $(1.00\pm0.01)\exp(\pm0.01i)$ and invert Eqs. (41) and (42), i.e.,

$$\psi_1=U(0,Z)\times1.01\exp(+0.01i)[\mathcal{B}(Z)+\mathcal{S}^-(Z)]\ , \tag{46}$$

$$\tilde{\mathcal{F}}_1(0)=U^{-1}(0,Z)\tilde{\mathcal{F}}(Z)-\mathcal{S}^+(0)\ , \tag{47}$$

$$\psi_2=U(0,Z)\times0.99\exp(-0.01i)[\mathcal{B}(Z)+\mathcal{S}^-(Z)]\ , \tag{48}$$

$$\tilde{\mathcal{F}}_2(0)=U^{-1}(0,Z)\tilde{\mathcal{F}}(Z)-\mathcal{S}^+(0)\ . \tag{49}$$

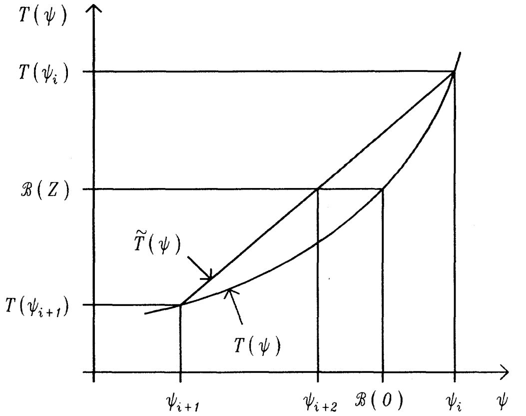

FIG. 2. An iterative secant approximation $\tilde{T}(\psi)$ of the nonlinear functional transformation $T(\psi)$ [Eq. (43)].

Of course, the bracketing in Fig. 2 is not necessary for the convergence of the foregoing "shooting-secant" algorithm. A rigorous mathematical assessment of the convergence may be very difficult to provide, not only because the algorithm on each characteristic base line is so intricate, but also because the iterations on separate base lines interact through the transverse Laplacian in Eqs. (31) and (32). I offer only the computations in Sec. IV as evidence of convergence. Because the transverse Laplacian connects the shootings on separate base lines, the shooting-secant iterations may not converge for a sufficiently large axial interval $(0,Z)$. For example, an iteration $\tilde{\mathcal{B}}(Z)$ may not be bracketed by the initial tolerances on the right-hand sides of Eqs. (46) and (48). Such a situation might improve if the iterations are reset by applying Eqs. (46)–(49) with the forward approximation $\tilde{\mathcal{F}}(Z)$ corresponding to $\tilde{\mathcal{B}}(Z)$, and there are other techniques for accelerating the convergence of secant estimation. Furthermore, the "diagonal" approximation in Eq. (45) could also be upgraded by including nondiagonal terms. If the interval $(0,Z)$ covers the whole laser, one is dealing essentially with a stochastic description of a steady-state laser. The x-ray laser is presently a nonstationary device whose simulation must include enough axial cells to resolve its temporal evolution adequately. None of the foregoing refinements is necessary for convergence of the calculations in Sec. IV.

4. Time and storage for two-way transport

Intervals of length Z [Eq. (36)] are linked together to complete the axial discretization for the laser. Let its length be l, and select integers M and N for which

$$(0,l)=(0,NZ)=(0,MNz)\quad (M,N=1,2,\ldots)\ . \tag{50}$$

Thus the fields are stored on $N+1$ transverse sections while MN axial steps of length z add up to the length of the laser. The time increment between adjacent transverse sections is $l\sqrt{\epsilon_a}/Nc$, which is larger than the conventional z-length increment $z\sqrt{\epsilon_a}/c$ when $M>1$. As long as the larger increment is satisfactory, the shooting-secant method is useful. It also can revert to the conventional advective strategy (i.e., no iteration) when $M=1$. Unlike the conventional strategy, the shooting-secant method allows axial refinement (increasing M) with no change in computing storage or the time increment (fixed N). Furthermore, a large reduction in storage can be achieved with less computing time.

In order to compare computing times, consider only a fixed number of transverse zones so that the computing time $\mathcal{T}_z$ per field per axial step of length z is the same. The number $\mathcal{I}_N$ of shooting-secant iterations needed for satisfactory convergence is small $(3\le\mathcal{I}_N\le5$ for the calculations in Sec. IV) and decreases slowly as N increases, i.e., as the interval $(0,Z)$ shortens. Also, let $K\ (=MN)$ be the number of z-length axial steps inside the laser.

The conventional computing strategy applies Eqs. (37) and (42) over K axial zones to advance the two fields $\mathcal{B}(z)$ and $\mathcal{F}(z)$ through one z-length step. This computation uses the time $2K\mathcal{T}_z$. If it is repeated K times, the fields advance an axial distance equaling the length of the laser. Letting $\mathcal{W}_{\rm CS}$ denote the total computing time for this conventional strategy, one concludes

$$\mathcal{W}_{\rm CS} \approx 2K^2\mathcal{T}_z\ . \tag{51}$$

The shooting-secant strategy applies Eq. (42) through M axial steps in each of N Z-length axial cells to get the N fields $\tilde{\mathcal{F}}(Z)$. This requires the time $MN\mathcal{T}_z$. Next, a computing time of $4MN\mathcal{T}_z$ is needed when Eqs. (46)–(49) are executed in the same way to get the initial guesses ψ_1 and ψ_2 in each of the Z-length axial cells. After these initial estimates are computed, one uses Eqs. (41) and (42) inside N Z-length axial cells to advance the two fields through one Z step. During this part of the calculation, M axial steps and $\mathcal{I}_N$ iterations are performed inside each Z-length cell, so this requires the time $2MN\mathcal{I}_N\mathcal{T}_z$. When such a calculation is repeated N times for a combined time of $2MN^2\mathcal{I}_N\mathcal{T}_z$, both fields advance a laser-length distance. Adding the initial-estimate time to this result yields the total shooting-secant time

$$\mathcal{W}_{\rm SS} \approx (2N\mathcal{I}_N+5)MN\mathcal{T}_z = (2KM^{-1}\mathcal{I}_N+5)K\mathcal{T}_z\ . \tag{52}$$

Equations (51) and (52) show that $\mathcal{W}_{\rm SS} < \mathcal{W}_{\rm CS}$ whenever

$$M > \mathcal{I}_N(1-\tfrac{5}{2}K^{-1})^{-1}\ , \tag{53}$$

an inequality that is readily satisfied. For example, some data in Sec. IV are $K=500$, $\mathcal{I}_N=3$, and $M=50$.

To advance the fields everywhere by one Z length, a calculation can proceed sequentially through the Z-length axial cells. This process requires the storage of the two successive approximations ψ_{i-1} and ψ_i [Eq. (45)] in addition to the backward and forward fields for a given cell. Since the storage for these approximations can be overwritten for each successive cell, the total storage for a sequential computation is $2(N+2)J$, where J equals the single-field storage in one transverse section. All the calculations in Sec. IV were obtained sequentially.

If there is sufficient storage to allocate the successive approximations ψ_{i-1} and ψ_i in each of the N Z-length cells, the shooting-secant algorithm can proceed parallelly in these cells. The total storage becomes $2(2N+1)J$, which is less than the conventional-strategy storage $2(MN+1)J$ when $M>2$. Thus the shooting-secant algorithm admits parallel computation in a very natural way. A large reduction in the sequential computing time should be relatively easy to achieve via parallel computation.

C. Transverse discretization

The discretization of the vacuum operator $\exp(\alpha\nabla_\perp^2 z)$ [Eq. (22)] can be done in many ways. Even though several authors have discussed this subject, I review it not only to explain the computations in Sec. IV, but also to point out certain aspects that, I feel, need further elucidation.

1. Transform methods

Equations (12), (15), and (22) indicate that the vacuum operator $\exp(\alpha\nabla_\perp^2 z)$ for one-transverse-dimensional Cartesian coordinates corresponds to the relation

$$\frac{\partial\psi}{\partial z} = \frac{i\lambda}{4\pi\sqrt{\epsilon_a}}\frac{\partial^2\psi}{\partial x^2}\ . \tag{54}$$

Take the Fourier transform

$$\tilde{\psi}(\alpha,z) = \int_{-\infty}^{\infty}\psi(x,z)\exp(-i2\pi\alpha x)dx \tag{55}$$

on each side of Eq. (54) to get

$$\frac{\partial\tilde{\psi}}{\partial z} = \frac{i\lambda}{4\pi\sqrt{\epsilon_a}}\int_{-\infty}^{\infty}\frac{\partial^2\psi}{\partial x^2}\exp(-i2\pi\alpha x)dx = -\frac{i\pi\lambda\alpha^2}{\sqrt{\epsilon_a}}\tilde{\psi}\ , \tag{56}$$

where the transverse boundary conditions in Eq. (13) have been used. Equation (56) can be integrated explicitly to yield the Fourier transform

$$\tilde{\psi}(\alpha,z) = \tilde{\psi}(\alpha,z_0)\exp\left[-\frac{i\pi\lambda\alpha^2}{\sqrt{\epsilon_a}}(z-z_0)\right]\ , \tag{57}$$

and, of course, the field ψ is the inverse transform

$$\psi(x,z) = \frac{1}{2\pi}\int_{-\infty}^{\infty}\tilde{\psi}(\alpha,z_0) \times \exp\left[i2\pi\alpha x - \frac{i\pi\lambda\alpha^2}{\sqrt{\epsilon_a}}(z-z_0)\right]d\alpha\ . \tag{58}$$

The unnormalized far-field angular distribution is obtained by the following substitution for the independent variable α of the Fourier transform:

$$\psi_{\rm FF}(\theta) = \tilde{\psi}(\sqrt{\epsilon_a}\,\theta/\lambda, z_0),\quad \theta = \frac{x}{z-z_0}\ . \tag{59}$$

A discrete Fourier transform (DFT) and a fast-Fourier transform (FFT) algorithm based on powers of 2 are popularly used to approximate the foregoing continuous Fourier-transform analysis. It is worthwhile to note that there are more general and very efficient FFT algorithms based on any highly factorable integer. Such algorithms greatly increase the selection available for the dimension of the transverse discretization, and this flexibility can be crucial when a computation strains the storage. For example, there are only the 13 powers 2^n $(n=1,2,\ldots,13)$ for which $2 \le 2^n \le 10\,000$, but 329 choices of the 4-set (i,j,k,l) are such that $2^i3^j5^k7^l$ satisfies this inequality.

When a computation taxes the storage, nonuniform transverse zoning can also be very useful. It permits an economy in which zones are clustered where there is more variation of the fields. One can also impose the transverse boundary conditions [Eq. (13)] much farther out into the wings of the transverse distribution. The Fourier-transform approach necessitates uniform zoning.

Perhaps the most useful feature of the DFT analog of Eq. (58) is that it allows a very efficient one-step calculation to any axial range whenever there is propagation through a uniform medium without gain or refraction. Such one-step computations can be done much less efficiently through a finite series of the following Gauss-Hermite modes [13], which constitute a complete and orthogonal set of solutions to Eq. (54):

$$\psi_0(x,z)=\pi^{-1/4}\sqrt{\sigma_0/\sigma}\,\exp\left\{-\frac{x^2}{\sigma^2}+i\frac{x^2}{\sigma^2}\frac{\lambda(z-z_0)}{\pi\sqrt{\epsilon_a}\sigma_0^2}-\frac{i}{2}\arctan\left[\frac{\lambda(z-z_0)}{\pi\sqrt{\epsilon_a}\sigma_0^2}\right]\right\}, \tag{60}$$

$$\psi_1(x,z)=2\frac{x}{\sigma}\psi_0(x,z)\exp\left\{-i\arctan\left[\frac{\lambda(z-z_0)}{\pi\sqrt{\epsilon_a}\sigma_0^2}\right]\right\}, \tag{61}$$

$$\psi_{n+1}(x,z)=\frac{2}{\sqrt{n+1}}\frac{x}{\sigma}\psi_n(x,z)\exp\left\{-i\arctan\left[\frac{\lambda(z-z_0)}{\pi\sqrt{\epsilon_a}\sigma_0^2}\right]\right\}-\left[\frac{n}{n+1}\right]^{1/2}\psi_{n-1}(x,z)\exp\left\{-2i\arctan\left[\frac{\lambda(z-z_0)}{\pi\sqrt{\epsilon_a}\sigma_0^2}\right]\right\} \quad (n=1,2,\dots)\,, \tag{62}$$

where

$$\sigma^2(z)=\sigma_0^2\left\{1+\left[\frac{\lambda(z-z_0)}{\pi\sqrt{\epsilon_a}\sigma_0^2}\right]^2\right\} \tag{63}$$

and

$$\int_{-\infty}^{\infty}\psi_m^*(x,z)\psi_n(x,z)\,d(\sqrt{2}x/\sigma)=\frac{\sigma_0}{\sigma}\delta_{mn}\,, \tag{64}$$

where δ_{mn} is Kronecker's delta. Every solution $\psi(x,z)$ of Eq. (54) can be represented by a series

$$\psi(x,z)=\sum_{n=0}^{\infty}c_n\psi_n(x,z) \tag{65}$$

in which the coefficients

$$c_n=\frac{\sigma}{\sigma_0}\int_{-\infty}^{\infty}\psi_n^*(x,z)\psi(x,z)\,d(\sqrt{2}x/\sigma) \quad (n=0,1,\dots) \tag{66}$$

are constants, i.e., are not dependent upon z. It follows from Eqs. (60)–(66) that the unnormalized far-field angular distribution is given by the following series with the same coefficients c_n:

$$\psi_{\mathrm{FF}}(\theta)=\sum_{n=0}^{\infty}c_n\phi_n(\theta),\quad \theta=\frac{x}{z-z_0}\,, \tag{67}$$

where

$$\phi_0(\theta)=\exp(-\pi^2\epsilon_a\sigma_0^2\lambda^{-2}\theta^2)\,, \tag{68}$$

$$\phi_1(\theta)=-2i\pi\sqrt{\epsilon_a}\sigma_0\lambda^{-1}\theta\phi_0(\theta)\,, \tag{69}$$

and

$$\phi_{n+1}(\theta)=-\left[\frac{2i\pi\sqrt{\epsilon_a}\sigma_0\lambda^{-1}}{\sqrt{n+1}}\right]\theta\phi_n(\theta)+\left[\frac{n}{n+1}\right]^{1/2}\phi_{n-1}(\theta) \quad (n=1,2,\dots)\,. \tag{70}$$

The integrals in Eqs. (66) can be calculated accurately by piecewise parabolic interpolation even when the grid is nonuniform, as long as it sufficiently resolves the transverse distribution of $\psi(x,z)$.

The rate of convergence of the series in Eq. (65) varies widely with the value of the spot-size parameter σ_0 in Eq. (63). There is, in fact, an optimal choice of σ_0. The width [14] of a Gauss-Hermite mode of index n is about $2\sqrt{n}\,\sigma_0$. The sum in Eq. (65) must include terms whose width equals or exceeds the width Γ of the distribution $\psi(x,z)$ so the maximum index N of a finite-series approximation of Eq. (65) must satisfy the inequality

$$\sqrt{N}\geq\frac{\Gamma}{2\sigma_0}\,. \tag{71}$$

Furthermore, the Gauss-Hermite mode of the maximum index N has about $N/2$ periods [14] across its full width $2\sqrt{N}\,\sigma_0$, so its period is about $4\sigma_0/\sqrt{N}$, which must not exceed the smallest period γ of the significant fluctuations of $\psi(x,z)$, i.e., $4\sigma_0/\sqrt{N}\leq\gamma$, or

$$\sqrt{N}\geq\frac{4\sigma_0}{\gamma}\,. \tag{72}$$

The right-hand sides of Eqs. (71) and (72) depend upon σ_0, respectively, in hyperbolically decreasing and linearly increasing fashions. The intersection of these curves, which occurs at the spot size

$$\sigma_0=\tfrac{1}{2}\sqrt{\gamma\Gamma/2} \tag{73}$$

yields the minimum index N that satisfies Eqs. (71) and (72) simultaneously. This minimum index corresponds to the optimal convergence of the sum in Eq. (65).

If the distribution $\psi(x,z)$ has a certain overall curvature to its phase, a proper choice of the waist-location parameter in Eq. (63) can also increase the rate of convergence in Eq. (65).

A one-step DFT calculation approximates the transverse distribution of $\psi(x,z)$ by a periodically extended function. Therefore, a one-step calculation to a large axial range breaks down if the field spreads beyond the grid boundaries. Then, an overlapping or "aliasing" from adjacent segments of the periodic function occurs. Of course, this difficulty can be avoided by accurately interpolating the field onto a larger grid before the onset of aliasing. Monotone piecewise-cubic interpolation [15] is particularly useful for this task because one obviously does not want to introduce extraneous oscillations or overshooting. However, it should also be realized that monotone interpolations of the real and imaginary parts of the field are not necessarily equivalent to monotone interpolations of its amplitude and phase. Monotone amplitude-phase interpolation onto a uniform grid is used in Sec. IV to obtain DFT far-field approximations from nonuniform-grid data.

The aliasing of a DFT approach does not occur in a Gauss-Hermite one-step calculation. If a finite-series approximation to Eq. (65) is sufficiently accurate when the field is confined inside the grid boundaries, accuracy over the grid remains if the field spreads beyond the grid boundaries—the solution merely "flows out" through them. Even though the Gauss-Hermite calculation is considerably less efficient than a DFT approach, the Gauss-Hermite avoidance of aliasing may be preferable, especially if the one-step calculation is a small part of the total calculation. The Gauss-Hermite method is too inefficient, however, to be practical for the many-step calculations inside the laser.

The cylindrically symmetric analog of Eq. (54) is

$$\frac{\partial\psi}{\partial z}=\frac{i\lambda}{4\pi\sqrt{\epsilon_a}}\frac{1}{r}\frac{\partial}{\partial r}\left[r\frac{\partial\psi}{\partial r}\right], \tag{74}$$

where $\psi(r,z)$ satisfies the transverse boundary conditions

$$\frac{\partial\psi}{\partial r}(0,z)=0,\quad \lim_{r\to\infty}\psi(r,z)=0\ . \tag{75}$$

The foregoing continuous Fourier-transform analysis of Eq. (54) [i.e., Eqs. (55)–(59)] translates into a continuous Hankel-transform analysis of Eq. (74). Unfortunately, despite considerable research, there seem to be no fast-Hankel-transform algorithms as satisfactory as the FFT algorithms for Eq. (54). Feit and Fleck's explicit fourth-order expansion [16], which avoids the Hankel transform altogether, is clearly unsuited for cylindrically symmetric long-range one-step calculations. Such calculations in Sec. IV rely upon Gauss-Laguerre analogs of Eqs. (60)–(70), even though the fast Hankel transforms are no doubt superior.

The Gauss-Laguerre modes of Eqs. (74) and (75) may be written in the form

$$\psi_0(r,z)=\frac{\sigma_0}{\sigma}\exp\left\{-\frac{r^2}{\sigma^2}+i\frac{r^2}{\sigma^2}\frac{\lambda(z-z_0)}{\pi\sqrt{\epsilon_a}\sigma_0^2}-i\arctan\left[\frac{\lambda(z-z_0)}{\pi\sqrt{\epsilon_a}\sigma_0^2}\right]\right\}, \tag{76}$$

$$\psi_1(r,z)=(1-2r^2\sigma^{-2})\psi_0(r,z)\exp\left\{-2i\arctan\left[\frac{\lambda(z-z_0)}{\pi\sqrt{\epsilon_a}\sigma_0^2}\right]\right\}, \tag{77}$$

$$\begin{aligned}\psi_{n+1}(r,z)={}&\left[\frac{2n+1-2r^2\sigma^{-2}}{n+1}\right]\psi_n(r,z)\exp\left\{-2i\arctan\left[\frac{\lambda(z-z_0)}{\pi\sqrt{\epsilon_a}\sigma_0^2}\right]\right\}\\&-\left[\frac{n}{n+1}\right]\psi_{n-1}(r,z)\exp\left\{-4i\arctan\left[\frac{\lambda(z-z_0)}{\pi\sqrt{\epsilon_a}\sigma_0^2}\right]\right\}\quad (n=1,2,\ldots)\ ,\end{aligned} \tag{78}$$

where $\sigma(z)$ is given by Eq. (63). These modes satisfy the orthogonality relations

$$\int_{-\infty}^{\infty}\psi_m^*(r,z)\psi_n(r,z)d(2r^2/\sigma^2)=\frac{\sigma_0^2}{\sigma^2}\delta_{mn}\ , \tag{79}$$

where δ_{mn} is Kronecker's delta, so every solution of Eqs. (74) and (75) has a series representation

$$\psi(r,z)=\sum_{n=0}^{\infty}c_n\psi_n(r,z) \tag{80}$$

with the constant coefficients

$$c_n=\frac{\sigma^2}{\sigma_0^2}\int_{-\infty}^{\infty}\psi_n^*(r,z)\psi(r,z)d(2r^2/\sigma^2)\qquad (n=0,1,\ldots)\ . \tag{81}$$

The far-field analogs of Eqs. (67)–(70) are

$$\psi_{\mathrm{FF}}(\theta)=\sum_{n=0}^{\infty}c_n\phi_n(\theta),\quad \theta=\frac{r}{z-z_0}\ , \tag{82}$$

where the coefficients c_n in Eqs. (80) and (82) are identical, $\phi_0(\theta)$ is given by Eq. (68), and

$$\phi_1(\theta)=-(1-2\pi^2\epsilon_a\sigma_0^2\lambda^{-2}\theta^2)\phi_0(\theta)\ , \tag{83}$$

$$\begin{aligned}\phi_{n+1}(\theta)={}&-\left[\frac{2n+1-2\pi^2\epsilon_a\sigma_0^2\lambda^{-2}\theta^2}{n+1}\right]\phi_n(\theta)\\&-\left[\frac{n}{n+1}\right]\phi_{n-1}(\theta)\quad (n=1,2,\ldots)\ .\end{aligned} \tag{84}$$

Piecewise parabolic interpolation leads to accurate evaluations of the integrals in Eq. (81), while Eq. (73) provides an optimum-convergence estimate of the spot-size σ_0 when the parameter Γ is interpreted to be the full width of the cylindrically symmetric distribution $\psi(r,z)$.

2. *Finite-difference methods*

A finite-difference discretization of Eq. (54) can closely parallel the usual treatments of the diffusion equation.

Let me discuss this subject within the framework of the well-known Hermitian method [17] for deriving high-accuracy finite-difference expressions. My goal is to arrive at results having the smallest truncation errors and adapted to nonuniform grids.

Consider first a semidiscrete analysis, continuous in z and having the not necessarily uniform grid x_i $(i=-n,-n+1,\ldots,n)$. Let the column vector

$$\boldsymbol{\psi}=[\psi(x_{-n},z),\psi(x_{-n+1},z),\ldots,\psi(x_n,z)]^T \tag{85}$$

denote the corresponding x discretization of a field $\psi(x,z)$ that is twice continuously differentiable in x and continuously differentiable in z. If the transverse extent of the grid is large enough in relation to the transverse distribution of $\psi(x,z)$, transverse boundary conditions like Eqs. (13) can be satisfied sufficiently well. If $\phi(x,z)$ is another continuous field, the two-point boundary-value problem

$$\frac{\partial^2\psi}{\partial x^2}=\phi\ , \tag{86}$$

$$A\psi(x_{-n},z)+B\frac{\partial\psi}{\partial x}(x_{-n},z)=0\quad(A^2+B^2>0)\ , \tag{87}$$

$$C\psi(x_n,z)+D\frac{\partial\psi}{\partial x}(x_n,z)=0\quad(C^2+D^2>0) \tag{88}$$

is well defined. The most general application of the Hermitian method yields $(2n+1)\times(2n+1)$ matrices $\underline{M}$ and $\underline{N}$ such that Eqs. (86)–(88) are approximated by the implicit finite-difference relations

$$\underline{M}\boldsymbol{\phi}=\underline{N}\boldsymbol{\psi}+O[(x_i-x_{i-1})^j]$$
$$(i=-n+1,-n+2,\ldots,n;\ j=1,2,\ldots)\ , \tag{89}$$

where the truncation errors generally decrease (i.e., j increases) as the number of nonzero elements in $\underline{M}$ and $\underline{N}$ increases.

The computations in Sec. IV involve only tridiagonal matrices $\underline{M}$ and $\underline{N}$, and $\underline{M}$ is also diagonally dominant. Therefore, $\underline{M}$ and $\underline{N}$ have relatively simple forms while $\underline{M}$ is particularly easy to invert. The matrices $\underline{M}$ and $\underline{N}$ are not uniquely determined by the Hermitian method. A convenient and elegant approach to tridiagonal Hermitian approximations first converts Eq. (86) into Rose's patch equations [18] for the interior points:

$$\int_{x_{i-1}}^{x_{i+1}}K_i(t)\phi(t,z)dt=\frac{\psi_{i+1}-\psi_i}{x_{i+1}-x_i}-\frac{\psi_i-\psi_{i-1}}{x_i-x_{i-1}}$$
$$(i=-n+1,-n+2,\ldots,n-1)\ , \tag{90}$$

where the kernels are

$$K_i(t)=\begin{cases}\dfrac{t-x_{i-1}}{x_i-x_{i-1}} & (x_{i-1}\le t\le x_i)\\[2ex] \dfrac{x_{i+1}-t}{x_{i+1}-x_i} & (x_i\le t\le x_{i+1})\end{cases}$$
$$(i=-n+1,-n+2,\ldots,n-1)\ . \tag{91}$$

A twice-repeated integration of Eq. (86) over the interval (x_{-n},x_{-n+1}) yields

$$\psi_{-n+1}=\psi_{-n}+\frac{\partial\psi_{-n}}{\partial x}(x_{-n+1}-x_{-n})$$
$$+\int_{x_{-n}}^{x_{-n+1}}dt\int_{x_{-n}}^{t}\phi(\mu,z)d\mu\ , \tag{92}$$

which may be integrated by parts and combined with Eq. (87) to furnish the integral boundary condition

$$A\psi_{-n}+B\left[\frac{\psi_{-n+1}-\psi_{-n}}{x_{-n+1}-x_{-n}}\right.$$
$$\left.-\int_{x_{-n}}^{x_{-n+1}}\frac{x_{-n+1}-t}{x_{-n+1}-x_{-n}}\phi(t,z)dt\right]=0\ , \tag{93}$$

Similar manipulations at the other boundary produce

$$C\psi_n+D\left[\frac{\psi_n-\psi_{n-1}}{x_n-x_{n-1}}+\int_{x_{n-1}}^{x_n}\frac{t-x_{n-1}}{x_n-x_{n-1}}\phi(t,z)dt\right]=0\ . \tag{94}$$

Rose's patch equations [i.e., Eq. (90)] are easily derived via a similar integration by parts coupled with the elimination of the first-order spatial derivative. Every solution of the continuous problem [Eqs. (86)–(88)] exactly satisfies these integral relations [Eqs. (90), (93), and (94)]. The discrete terms in these expressions make up the elements of $\underline{N}$. Constant, linear, and parabolic interpolation of ϕ inside the integral terms determines the elements of $\underline{M}$.

If the integral in Eq. (90) is approximated by constant interpolation,

$$\int_{x_{i-1}}^{x_{i+1}}K_i(t)\phi(t,z)dt\approx\phi_i\int_{x_{i-1}}^{x_{i+1}}K_i(t)dt=\frac{l_{i-1}+l_i}{2}\phi_i\ , \tag{95}$$

where

$$l_i=x_{i+1}-x_i\ . \tag{96}$$

Equations (90) and (95) thus provide the finite-difference expression

$$\frac{l_{i-1}+l_i}{2}\phi_i=\frac{\psi_{i+1}-\psi_i}{l_i}-\frac{\psi_i-\psi_{i-1}}{l_{i-1}}\ , \tag{97}$$

which has the constant-interpolation truncation error

$$\mathcal{T}_c=\frac{1}{3}\left[\frac{l_i^2-l_{i-1}^2}{l_{i-1}+l_i}\right]\phi_i^{(1)}+\frac{1}{12}\left[\frac{l_{i-1}^3+l_i^3}{l_{i-1}+l_i}\right]\phi_i^{(2)}+\cdots\ . \tag{98}$$

Equation (97) reduces to the usual central-difference estimate when the grid is uniform. Note that this truncation error, which is second-order for a uniform grid, is not even first-order when the grid is nonuniform.

If ϕ is linearly interpolated, i.e.,

$$\phi \approx \begin{cases} \dfrac{x_i - x}{x_i - x_{i-1}}\phi_{i-1} + \dfrac{x - x_{i-1}}{x_i - x_{i-1}}\phi_i \quad (x_{i-1} \le x \le x_i) \\ \dfrac{x_{i+1} - x}{x_{i+1} - x_i}\phi_i + \dfrac{x - x_i}{x_{i+1} - x_i}\phi_{i+1} \quad (x_i \le x \le x_{i+1}) \ , \end{cases} \tag{99}$$

Eq. (90) leads to the implicit relation

$$\frac{l_{i-1}}{6}\phi_{i-1} + \frac{l_{i-1}+l_i}{3}\phi_i + \frac{l_i}{6}\phi_{i+1} = \frac{\psi_{i+1}-\psi_i}{l_i} - \frac{\psi_i - \psi_{i-1}}{l_{i-1}} \ . \tag{100}$$

The associated linear-interpolation truncation error is

$$\mathcal{T}_l = -\frac{1}{12}\left[\frac{l_{i-1}^3 + l_i^3}{l_{i-1}+l_i}\right]\phi_i^{(2)} + \cdots \ , \tag{101}$$

which is second-order whether the grid is uniform or nonuniform.

The smallest truncation errors are obtained by parabolic interpolation. Consider boundary conditions in which the gradients vanish [i.e., $A = C = 0$ in Eqs. (87) and (88)], and approximate ϕ by the piecewise parabolas

$$\phi \approx \frac{(x_{-n+1} - x_{-n})^2 - (x - x_{-n})^2}{(x_{-n+1} - x_{-n})^2}\phi_{-n} + \left[\frac{x - x_{-n}}{x_{-n+1} - x_n}\right]^2 \phi_{-n+1} \quad (x_{-n} \le x \le x_{-n+1}) \ , \tag{102}$$

$$\phi \approx \frac{x - x_i}{x_i - x_{i-1}}\,\frac{x - x_{i+1}}{x_{i+1} - x_{i-1}}\phi_{i-1} + \frac{x - x_{i-1}}{x_i - x_{i-1}}\,\frac{x_{i+1} - x}{x_{i+1} - x_i}\phi_i + \frac{x - x_{i-1}}{x_{i+1} - x_{i-1}}\,\frac{x - x_i}{x_{i+1} - x_i}\phi_{i+1}$$
$$(x_{i-1} \le x \le x_{i+1};\ i = -n+1, -n+2, \ldots, n-1) \ , \tag{103}$$

$$\phi \approx \left[\frac{x_n - x}{x_n - x_{n-1}}\right]^2 \phi_{n-1} + \frac{(x_n - x_{n-1})^2 - (x_n - x)^2}{(x_n - x_{n-1})^2}\phi_n \quad (x_{n-1} \le x \le x_n) \ . \tag{104}$$

Then Eqs. (90), (93), and (94) generate the following implicit finite-difference relations:

$$\frac{5l_{-n}}{12}\phi_{-n} + \frac{l_{-n}}{12}\phi_{-n+1} = \frac{\psi_{-n+1} - \psi_{-n}}{l_{-n}} \ , \tag{105}$$

$$\frac{1}{6(l_{i-1}+l_i)}\left[l_{i-1}\left[\frac{l_{i-1}}{2} + l_i\right] - \frac{l_i^3}{2l_{i-1}}\right]\phi_{i-1} + \frac{1}{3}\left[l_{i-1}\left[1 + \frac{l_{i-1}}{4l_i}\right] + l_i\left[1 + \frac{l_i}{4l_{i-1}}\right]\right]\phi_i$$
$$+ \frac{1}{6(l_{i-1}+l_i)}\left[l_i\left[l_{i-1} + \frac{l_i}{2}\right] - \frac{l_{i-1}^3}{2l_i}\right]\phi_{i+1} = \frac{\psi_{i+1} - \psi_i}{l_i} - \frac{\psi_i - \psi_{i-1}}{l_{i-1}} \quad (i = -n+1, -n+2, \ldots, n-1) \ , \tag{106}$$

$$\frac{l_{n-1}}{12}\phi_{n-1} + \frac{5l_{n-1}}{12}\phi_n = -\frac{\psi_n - \psi_{n-1}}{l_{n-1}} \ . \tag{107}$$

The truncation error of Eq. (106) is

$$\mathcal{T}_p = -\tfrac{1}{36}(l_i^3 - l_{i-1}^3)\phi_i^{(3)} - \tfrac{1}{720}(3l_{i-1}^4 + 2l_{i-1}^3 l_i - 7l_{i-1}^2 l_i^2 + 2l_{i-1} l_i^3 + 3l_i^4)\phi_i^{(4)} + \cdots \ , \tag{108}$$

which is third order for a nonuniform grid and fourth order for a uniform grid. For the simplest second-order differential operator in Eq. (86), the differential and integral Hermitian procedures lead to the same finite-difference expressions. In general, however, the two methods generate different approximations. The uniform fourth-order error in Eq. (108) is exceptional—tridiagonal differential Hermitian estimates generally yield no smaller than third-order errors [17].

The integral Hermitian method is especially useful for curvilinear coordinates. Consider a cylindrically symmetric analog of the two-point boundary-value problem in Eqs. (86)–(88), i.e.,

$$\frac{1}{r}\frac{\partial}{\partial r}\left[r\frac{\partial\psi}{\partial r}\right] = \phi \ , \tag{109}$$

$$\frac{\partial\psi}{\partial r}(0,z) = 0 \ , \tag{110}$$

$$\frac{\partial\psi}{\partial r}(r_n,z) = 0 \ . \tag{111}$$

The cylindrically symmetric analog of the Cartesian integral boundary conditions [Eqs. (93) and (94)] have the forms

$$\psi_1 - \psi_0 = \int_0^{r_1} t\,\ln(r_1/t)\phi(t,z)dt \ , \tag{112}$$

$$\psi_n - \psi_{n-1} = -\int_{r_{n-1}}^{r_n} t\,\ln(t/r_{n-1})\phi(t,z)dt \ . \tag{113}$$

Rose's patch equations [18] for the interior points are

$$\int_0^{r_2} tK_1(t)\phi(t,z)dt=\psi_2-\psi_1\ , \tag{114}$$

$$\int_{r_{i-1}}^{r_{i+1}} tK_i(t)\phi(t,z)dt=\frac{\psi_{i+1}-\psi_i}{\ln(r_{i+1}/r_i)}-\frac{\psi_i-\psi_{i-1}}{\ln(r_i/r_{i-1})} \quad (i=2,3,\ldots,n-1)\ , \tag{115}$$

where the kernels are

$$K_1(t)=\begin{cases}\ln(r_2/r_1) & (0\le t\le r_1)\\ \ln(r_2/t) & (r_1\le t\le r_2)\ ,\end{cases} \tag{116}$$

$$K_i(t)=\begin{cases}\dfrac{\ln(t/r_{i-1})}{\ln(r_i/r_{i-1})} & (r_{i-1}\le t\le r_i)\\[2ex] \dfrac{\ln(r_{i+1}/t)}{\ln(r_{i+1}/r_i)} & (r_i\le t\le r_{i+1})\end{cases} \quad (i=2,3,\ldots,n-1)\ . \tag{117}$$

Parabolic interpolation in Eqs. (112)–(115) gives the following finite-difference equations:

$$\frac{3r_1^2}{16}\phi_0+\frac{r_1^2}{16}\phi_1=\psi_1-\psi_0\ , \tag{118}$$

$$-\frac{(r_2^2-r_1^2)(7r_1^2-20r_1r_2+7r_2^2)}{144r_1r_2}\phi_0+\frac{9r_1^4-16r_1^3r_2+7r_2^4}{144r_1(r_2-r_1)}\phi_1+\frac{7r_1^4-16r_1r_2^3+9r_2^4}{144r_2(r_2-r_1)}\phi_2=\psi_2-\psi_1\ , \tag{119}$$

$$\begin{aligned}
&\left\{\frac{r_{i+1}-r_i}{\ln(r_{i+1}/r_i)}[9(r_{i+1}^4-r_i^4)-16(r_i+r_{i+1})(r_{i+1}^3-r_i^3)+36r_ir_{i+1}(r_{i+1}^2-r_i^2)]\right.\\
&\qquad\left.-\frac{r_{i+1}-r_i}{\ln(r_i/r_{i-1})}[9(r_i^4-r_{i-1}^4)-16(r_i+r_{i+1})(r_i^3-r_{i-1}^3)+36r_ir_{i+1}(r_i^2-r_{i-1}^2)]\right\}\phi_{i-1}\\
&\quad+\left\{\frac{r_{i+1}-r_{i-1}}{\ln(r_i/r_{i-1})}[9(r_i^4-r_{i-1}^4)-16(r_{i+1}+r_{i-1})(r_i^3-r_{i-1}^3)+36r_{i-1}r_{i+1}(r_i^2-r_{i-1}^2)]\right.\\
&\qquad\left.-\frac{r_{i+1}-r_{i-1}}{\ln(r_{i+1}/r_i)}[9(r_{i+1}^4-r_i^4)-16(r_{i+1}+r_{i-1})(r_{i+1}^3-r_i^3)+36r_{i-1}r_{i+1}(r_{i+1}^2-r_i^2)]\right\}\phi_i\\
&\quad+\left\{\frac{r_i-r_{i-1}}{\ln(r_{i+1}/r_i)}[9(r_{i+1}^4-r_i^4)-16(r_i+r_{i-1})(r_{i+1}^3-r_i^3)+36r_{i-1}r_i(r_{i+1}^2-r_i^2)]\right.\\
&\qquad\left.-\frac{r_i-r_{i-1}}{\ln(r_i/r_{i-1})}[9(r_i^4-r_{i-1}^4)-16(r_i+r_{i-1})(r_i^3-r_{i-1}^3)+36r_{i-1}r_i(r_i^2-r_{i-1}^2)]\right\}\phi_{i+1}\\
&\qquad\qquad=144(r_i-r_{i-1})(r_{i+1}-r_i)(r_{i+1}-r_{i-1})\left[\frac{\psi_{i+1}-\psi_i}{\ln(r_{i+1}/r_i)}-\frac{\psi_i-\psi_{i-1}}{\ln(r_i/r_{i-1})}\right] \quad (i=2,3,\ldots,n-1)\ ,
\end{aligned} \tag{120}$$

$$\begin{aligned}
&[13r_n^4-36r_n^2r_{n-1}^2+32r_nr_{n-1}^3-9r_{n-1}^4-12r_n^4\ln(r_n/r_{n-1})]\phi_{n-1}+[9r_n^4-32r_n^3r_{n-1}+36r_n^2r_{n-1}^2\\
&\qquad-13r_{n-1}^4-12r_n^2(3r_n^2-8r_nr_{n-1}+6r_{n-1}^2)\ln(r_n/r_{n-1})]\phi_n=144(r_n-r_{n-1})^2(\psi_n-\psi_{n-1})\ .
\end{aligned} \tag{121}$$

The foregoing semidiscrete analysis approximates Eqs. (54) and (74) by relations of the form

$$\frac{d\boldsymbol{\psi}}{dz}=i\alpha[\underline{M}^{-1}\underline{N}+O(\Delta^m)]\boldsymbol{\psi} \quad (m=0,1,2,3,4)\ , \tag{122}$$

where Δ is a transverse spatial increment and $\alpha=\lambda/(4\pi\sqrt{\epsilon_a})$. If one introduces an axial discretization having the constant step z and labeled by the superscript n, the exact solution of Eq. (122) can be approximated by an axially centered two-level scheme:

$$\begin{aligned}
\boldsymbol{\psi}^{n+1}&=\exp\{i\alpha z[\underline{M}^{-1}\underline{N}+O(\Delta^m)]\}\boldsymbol{\psi}^n\\
&=\left\{\underline{I}-\frac{i\alpha z}{2}\left[\underline{M}^{-1}\underline{N}+O(\Delta^m)\right]\right\}^{-1}\\
&\quad\times\left\{\underline{I}+\frac{i\alpha z}{2}\left[\underline{M}^{-1}\underline{N}+O(\Delta^m)\right]\right\}\boldsymbol{\psi}^n+O(z^3)\ ,
\end{aligned} \tag{123}$$

which implies that

$$\left[\underline{M}-\frac{i\alpha z}{2}\underline{N}\right]\psi^{n+1}=\left[\underline{M}+\frac{i\alpha z}{2}\underline{N}\right]\psi^{n}+O(z^3+z\Delta^m)$$
$$(m=0,1,2,3,4)\ . \qquad (124)$$

The different truncation errors in Eq. (124) arise from the accuracy of the various integral interpolations leading to the matrix $\underline{M}$—the tridiagonal matrix $\underline{N}$ is the same for all these interpolations. Constant interpolation produces a diagonal $\underline{M}$. With linear or parabolic interpolation, $\underline{M}$ is tridiagonal and has more complex elements. After the initial computation of these elements, the extra computing burden of the higher-order interpolations is insignificant. Therefore, as long as the solution of the continuous problem has continuous derivatives of a high enough order to justify higher-order interpolation, it is worthwhile to use such interpolation. All the finite-difference computations in Sec. IV use parabolic-interpolation formulas for nonuniform grids.

3. Comments on various methods

Numerous authors use tridiagonal finite-difference approximations of lesser accuracy and/or flexibility. Garrison *et al.* [5] and Scarmozzino and Osgood [19] estimate second-order derivatives by the usual three-point central-difference formula—constant integral interpolation restricted to a uniform grid. Fleck's analysis [20] based on "cylindrical cubic splines" is equivalent to linear integral interpolation over an arbitrary grid, but his treatment loses efficiency and wastes storage because it introduces unnecessary intermediate steps involving spline coefficients.

No tridiagonal finite-difference algorithm like Eq. (124) can match the accuracy of the corresponding DFT-FFT procedure outlined in Eqs. (54)–(59). However, this greater accuracy may have little consequence for the split-operator numerical solution of Eq. (17) because the splitting of the operators in Eqs. (20) and (21) incurs an error of order $O(z^3)$. In most cases, this error is large enough to obscure any benefit arising from the extra accuracy of the DFT-FFT calculation. There are exceptions, however. If the coefficient β in Eq. (17) is sufficiently small in relation to the coefficient α in the same equation (as it can be, for example, in atmospheric propagation), the splitting error of order $O(z^3)$ is relatively small even with large axial steps. Then the DFT-FFT method, which permits arbitrarily large axial steps through a uniform medium, also allows much larger steps through a near-uniform medium and thereby performs more efficiently. On the other hand, the coefficient β for x-ray lasers is much larger so that the added accuracy of a DFT-FFT calculation has a rather marginal effect on the overall computation.

This conclusion—that the split-operator DFT-FFT calculation is marginally more accurate than the split-operator parabolic-interpolation finite-difference (PIFD) approach—does not contradict the findings of Scarmozzino and Osgood [19], who determine for their integrated-optics applications that their finite-difference technique offers an order-of-magnitude improvement over the DFT-FFT method. Their finite-difference analysis eliminates the splitting of operators whereas a standard DFT-FFT calculation cannot do so because of the space-dependent coefficients in their applications. This difference skews the comparison in favor of their finite differences. They consider a more general problem than Eq. (54), namely

$$\frac{\partial\psi}{\partial z}=\alpha(x,z)\frac{\partial^2\psi}{\partial x^2}+\beta(x,z)\psi\ . \qquad (125)$$

Equation (86) generalizes to the form

$$\alpha\frac{\partial^2\psi}{\partial x^2}+\beta\psi=\phi\ , \qquad (126)$$

and the foregoing integral Hermitian analysis generates *different* matrices $\underline{M}$ and $\underline{N}$ inside Eq. (124), which then approximates the propagation without the errors of operator splitting. Moreover, calculating the matrix elements via parabolic interpolation would yield smaller transverse truncation errors than the central-difference approximations used by Scarmozzino and Osgood [19].

The elimination of operator splitting is not possible for a standard DFT-FFT approach whenever there are space-dependent and/or field-dependent coefficients. However, Feit and Fleck's explicit fourth-order expansion [16] of the evolution operator on the right-hand side of Eq. (17) avoids operator splitting and still permits FFT computation. Because their method is explicit, the size of the axial steps is strictly limited by considerations of conditional stability and accuracy. Such restrictions may be inconsequential when the coefficient β in Eq. (17) is large enough to dictate small axial steps. It would be especially interesting to compare their method to a cylindrically symmetric analog of Scarmozzino and Osgood's study [19].

When space-dependent refraction and nonlinear gain are in effect, the coefficient β in Eq. (17) depends explicitly upon the transverse coordinate and the field. In the lowest approximation, the elimination of operator splitting yields the following generalization of Eq. (124):

$$\left[\underline{M}-\frac{i\alpha z}{2}\underline{N}-\frac{z}{2}\underline{M}\,\underline{D}\right]\psi^{n+1}=\left[\underline{M}+\frac{i\alpha z}{2}\underline{N}+\frac{z}{2}\underline{M}\,\underline{D}\right]\psi^{n}\ , \qquad (127)$$

where the diagonal matrix $\underline{D}$ has the nonzero entries $\beta(x_i,\psi_i^n)$ $(i=-n,-n+1,\ldots,n)$. Because of the parabolic integral interpolation, the matrices $\underline{M}$ and $\underline{N}$ implicitly provide high-accuracy tridiagonal representations of the derivative $\partial^2/\partial x^2$ when there is no refraction or gain. On the other hand, the accuracy of Eq. (127) is reduced because the matrix $\underline{D}$ represents refraction and gain only diagonally. Complicated coefficients like those in Eqs. (118)–(121), arising from an analytical evaluation of Hermitian integrals, certainly tax one's patience and/or tolerance for complexity. However, such integrals can be evaluated numerically. Because the practical accuracy of finite-difference expressions is relatively insensitive to how accurately their coefficients are evaluated, the Hermitian integrals require only modestly accurate evaluation. Therefore, to obtain tridiagonal estimates with the greatest possible practical accuracy, the analytical PIFD can be replaced by its numerical implementation, applied to the entire right-hand side of Eq. (17), and imposed at sufficiently regular axial intervals when its coefficients depend explicitly upon the axial and dependent variables. Instead of speculating about the resulting accuracy and/or efficiency, I defer further comment until ongoing work is completed.

Another economy is possible for problems requiring sufficiently small axial steps. A CRAY-Y/MP8 central-processor time needed to evaluate $\exp(z)$ is 8–9% greater than the computing time for its third-order approximation $(1-\frac{1}{2}z)^{-1}(1+\frac{1}{2}z)$. One expects a similar comparison for the "diagonal" exponential operators in Eqs. (20) and (21). Furthermore, Sec. IV illustrates that the central-processor time for the exponential factors exceeds the time for a DFT-FFT or PIFD vacuumlike step by a factor ranging between 4 and 8, i.e., most of the computing time (76–89%) is used to compute the exponential terms. Replacing the exact exponentials by their third-order approximations, which are accurate for sufficiently small axial steps, can therefore save an appreciable amount of computing time.

There is also another issue in comparing the DFT-FFT and PIFD methods. Scarmozzino and Osgood [19], working on a personal computer, observe that their finite-difference computing time per axial step is 10–20% less than the corresponding DFT-FFT step when $64 \leq N \leq 1024$. The number of arithmetic operations in a DFT-FFT step is proportional to $N \ln N$ whereas a PIFD step such as Eq. (124) needs only N operations. Therefore, one expects a PIFD step to require less computing time than a DFT-FFT step when N is sufficiently large. However, Sec. IV displays a typical CRAY-Y/MP8 calculation in which a PIFD step requires about twice as much computing time as a DFT-FFT step even when $N=5760$ (which has the highly factorable form $2^7 \times 3^2 \times 5$ so that the DFT-FFT computation is efficient). Any comparison of computing methods should obviously consider factors other than the number of arithmetic operations—for example, the relative efficiencies of DFT-FFT versus PIFD algorithms may depend upon how well these algorithms can be vectorized.

The computer codes behind the results in Sec. IV are based upon the splitting of operators and the evaluation of exact exponentials. These codes can easily be adapted to third-order expansions of the exponentials or the elimination of operator splitting. Because of the fairly wide range of the electron density, the coefficient β in Eq. (17) is relatively large. Therefore, Eq. (127) is also checked to see whether it yields, like the results of Scarmozzino and Osgood [19], significant improvements in speed and/or accuracy. Even though a non-split-operator approach sidesteps the axial error of order $O(z^3)$ in Eq. (21), an axial error of the same order emerges from the axial-centered two-level expansion in Eq. (123). Thus the finite-difference algorithm in Eq. (127) can be less efficient for reasons besides the low accuracy arising from the diagonal matrix $\underline{D}$.

D. Miscellany

1. Free-electron density and small-signal gain

Section IV uses either a parabola or a Gaussian function to model the free-electron density n_e [Eq. (1)]:

$$n_e(x)=\begin{cases} n_e(0)(1-4x^2/w^2) & (|x| \leq w/2) \\ 0 \quad (|x| > w/2) \,, & \end{cases} \tag{128}$$

$$n_e(x)=n_e(0)\exp(-4x^2/w^2) \,, \tag{129}$$

where w is the width of the laser. The derivative of the parabolic distribution has an unphysical discontinuity at the edge of the laser. Since a first-order Taylor series of the exponential function equals the parabola inside the laser, the exponential distribution matches the parabola near the center of the laser and replaces the foregoing discontinuity by a smoothly decaying variation at the laser's edge.

The small-signal gain g_0 [Eq. (9)] is also modeled by the parabolic or exponential distributions in Eqs. (128) and (129).

2. Spontaneous-emission modeling

The spontaneous-emission amplitude $A^{\pm}$ [Eq. (10)] is simulated in two ways: (a) $A^{\pm}$ has the profile of the small-signal gain [Eq. (9)] and a maximum equal to a constant A; and (b) $A^{\pm}$ equals a constant A inside the laser and rapidly decays outside the laser via the function

$$A^{\pm}=\begin{cases} A\exp\left[-\dfrac{(x+w/2)^2}{\xi^2 w^2}\right] & (-\infty < x < -w/2) \\ A \quad (-w/2 \leq x \leq w/2) & \\ A\exp\left[-\dfrac{(x-w/2)^2}{\xi^2 w^2}\right] & (w/2 < x < \infty) \,, \end{cases} \tag{130}$$

where w is the width of the laser, and where the parameter ξ $(=5.43\times 10^{-4})$ is chosen so that the field intensity is reduced by the factor 10^{-4} at a distance from the edge of the laser equal to $w/20$. Either specification of the amplitude ensures that all the spontaneous-emission increments have the same power.

The phases $\Phi^{\pm}$ [Eq. (10)] of the spontaneous emission are selected randomly by a real sequence of pseudorandom numbers. This sequence is associated with a set of phase gridpoints that is less dense than the transverse grid. A standard cubic spline, satisfying the boundary conditions that its first derivative vanishes at its end points, is passed through the phase grid and used to interpolate the phase curve onto the transverse grid. If the phase grid is sufficiently less dense than the transverse grid, one obtains stochastic phase curves leading to smooth transverse Laplacians [Eq. (12)]. The calculations in Sec. IV indicate that this stochastic modeling of the phase produces a rather uniform spectral distribution over all modes up to a maximum frequency that increases with the density of the phase grid.

The amplitude A [Eq. (130)] of the spontaneous-emission increments must vary with the number of axial cells N [Eq. (50)] in order that the total spontaneous emission be fixed. Even though the gain of the laser is saturable, it is approximately linear over small cells. The relationship between amplitudes for different cells may therefore be characterized as a random walk with linear gain. Let A and a denote, respectively, the amplitude of a large cell and the common amplitude of n small cells that refine the large cell. Because the spontaneous emission is random, the amplitude A and the n random-phase amplitudes a satisfy the usual relation

$$A^2 = na^2 , \tag{131}$$

where there is no gain. If a field $\psi(0)$ undergoes "linearized" gain in accordance with Eqs. (9) and (12), its amplitude at the end of an axial increment of length z is

$$\psi(z) \approx \psi(0)\exp(gz/2) . \tag{132}$$

Thus, if the amplitude A is injected at the beginning of a cell of length nz, it grows to the squared amplitude $A^2\exp(ngz)$ at the end of the cell. If the small amplitude a is injected at the axial position mz $(m<n)$, it grows only to the squared amplitude $a^2\exp[(n-m)gz]$ at the end of the cell. If the output from the injection of amplitude A equals the output from n distributed and random-phase injections of amplitude a,

$$A^2\exp(ngz) = a^2\exp(gz) + a^2\exp(2gz) + \cdots + a^2\exp(ngz) . \tag{133}$$

Summing the geometric series on the right-hand side of Eq. (133) indicates that

$$A^2 = \frac{[1-\exp(-ngz)]}{[1-\exp(-gz)]}a^2 \equiv F(n,g,z)a^2 , \tag{134}$$

which represents a linear-gain generalization of Eq. (131) since

$$\lim_{g\to 0} F(n,g,z) = n . \tag{135}$$

Equation (134) is used in Sec. IV to provide approximately equal amounts of spontaneous emission in calculations with different axial cells.

3. *Coherence calculations*

Anticipated applications of x-ray lasers require a sufficiently high degree of coherence. Although the temporal (or longitudinal) coherence of x-ray lasers is expected to be satisfactory, their transverse (or spatial) coherence needs to be improved by narrowing their width, increasing their gain length, and avoiding gain saturation as much as possible [7]. Section IV includes calculations of the complex coherence factor [4,5,21,22]

$$\mu(x) \equiv \frac{\langle \mathcal{E}^*(0,l,t)\mathcal{E}(x,l,t)\rangle}{[\langle|\mathcal{E}(0,l,t)|^2\rangle\langle|\mathcal{E}(x,l,t)|^2\rangle]^{1/2}} \quad (-w/2 \le x \le w/2) , \tag{136}$$

where w is the width of the laser, $\mathcal{E}(x,l,t)$ is the paraxial field at the output of the laser, and the angular brackets $\langle\ \rangle$ denote a time average. An analytic investigation of coherence via modal analyses is rather difficult even with linearized approximation (i.e., unsaturated gain) [23,24]. Of course, the calculation in Eq. (136) is an easy addendum to any detailed numerical simulation [4,5,25].

After the sources of spontaneous emission are "switched on," the laser's evolution is nonstationary until forward and backward waves propagate many times through the laser. Then the gain-saturation term in Eq. (12) "settles down" as the stochastically driven laser evolves into a stationary random process, which takes about four or five laser-transit times to establish. When the laser is nonstationary, the angular brackets $\langle\ \rangle$ in Eq. (136) should really denote an ensemble average, whose computation is much more involved than a time average of the laser's output. The gain probably subsides before the passage of five laser-transit times so a serious calculation of coherence should really be nonstationary. The difficulty and large cost of nonstationary calculations, considered in relation to the computational economies provided by the iterative methods in Sec. III B, make those methods all the more valuable.

IV. CALCULATIONS AND DISCUSSION

The computations below are selected in accord with three purposes: (a) to illustrate and/or justify various remarks and analyses in what precedes; (b) to ascertain some deficiencies in previous work; and (c) to discuss certain properties of the x-ray output. The discussion focuses on the exploding-foil Ne-like selenium laser—collisionally excited $3p$ and $3s$ levels, and inverted on the $3p$-$3s$ transition by virtue of the fast radiative decay of the $3s$ level to ground. All that follows derives from Table I and certain variations of its data.

A. One-way calculations

Relatively inexpensive one-way computations provide much insight for modeling x-ray lasers.

1. *Sufficiently dense grids*

Let me first determine how dense a grid must be to get convergence with the data in Table I. Consider a family of calculations, differing in the number of axial steps, but having in common the following features:

(a) An xz Cartesian geometry describes the amplifier.

(b) There is no spontaneous emission inside the amplifier.

(c) The free-electron density and the gain have the parabolic distributions associated with Eq. (128) and Table I.

(d) The steady-state Gaussian beam $\psi(x,0) = A\exp[-(x/0.01)^2]$ enters the amplifier (A is given by Table I while the waist of the beam is located at $z=0$).

(e) To allow for diffractive and refractive expansion of the beam beyond the transverse boundaries of the amplifier, the transverse grid uniformly covers the interval $(-4.000\times10^{-2}, 4.015\times10^{-2})$ with 5760 $(=2^7\times3^2\times5)$ points.

TABLE I. Parameters for the exploding-foil Ne-like selenium laser [3,4,26].

Quantity	Symbol	Value	Equation References
Spontaneous-emission amplitude[a]	A	8.682×10^{-3} V cm^{-1}	Eqs. (10) and (130)
Small-signal-gain amplitude	$g_0(0)$	6.000 cm^{-1}	Eqs. (9), (128), and (129)
Saturation intensity[b]	I_{sat}	3.950 W cm^{-2}	Eqs. (9) and (11)
Amplifier length	l	4.000 cm	Eqs. (50) and (136)
Free-electron-density amplitude	$n_e(0)$	5.000×10^{20} cm^{-3}	Eqs. (1), (128), and (129)
Amplifier width	w	4.000×10^{-2} cm	Eqs. (128)–(130)
Average permittivity[c]	ϵ_a	9.999×10^{-1}	Eqs. (1) and (2)
Wavelength	λ	2.000×10^{2} Å	Eqs. (3), (12), (54), and (74)

[a] This datum corresponds to an intensity of 1.000×10^{-7} W cm^{-2}.

[b] This datum was selected to yield a transversely averaged two-way axial-gain curve similar to recent work discussed in the two-way calculations below. One can infer from Eqs. (11) and (12) that the variables A and I_{sat} enter the computations only through the ratio $A/\sqrt{I_{\text{sat}}}$.

[c] The value $n_e=2.5\times10^{20}$ cm^{-3}, used to calculate ϵ_a, is the average of the minimum and maximum of the free-electron-density distribution given by Eqs. (128) and (129) and the datum above for $n_e(0)$.

(f) The computations use the one-way time-independent split-operator DFT-FFT method (Sec. III), which is efficient because of the highly factorable transverse discretization just mentioned.

Figure 3 overlaps the near-field intensities computed with 100, 200, 300, 400, 500, and 1000 axial steps. A curve for 2000 axial steps overlaps the 1000-step curve so closely that their separation is barely discernible. Thus it is clear that at least 500 steps, and preferably 1000 steps, are required to obtain reasonably converged results (Feit and Fleck [4] use only 100 axial steps).

Surfaces of constant phase, corresponding to the near-field intensities in Fig. 3, are plotted in Fig. 4. It is again clear that at least 500 steps are needed for satisfactory convergence.

The converging near-field intensities of Fig. 3 widen as their peaks diminish and eventually disappear. Since the far-field angular distribution equals a certain rescaled Fourier transform of the near field [Eq. (59)], one expects, because of the uncertainty relations for the widths of Fourier-transform pairs, that the corresponding far-field distributions are successively narrower. Figure 5 confirms such a relationship and indicates that the converged far-field angular distribution has prominent spikes at about $\pm1.38\times10^{-2}$ rad.

The smoothness of the curves in Figs. 3 and 4 might foster a mistaken impression that the uniform transverse grid of 5760 points is far denser than what is necessary. This zoning density is, in fact, rather modest. The curves of Fig. 4 are constructed in the following way. In order to determine the phase of the field, the computed phase $\phi(x,z)$ of the paraxial envelope must be added to the

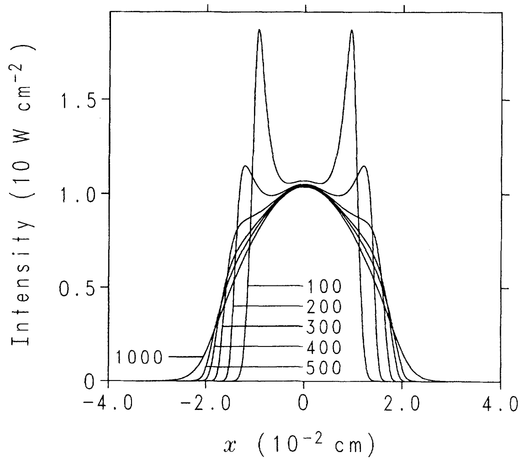

FIG. 3. Near-field intensities of a steady-state Gaussian beam passing through an exploding-foil Ne-like selenium amplifier. The various curves are labeled with the number of axial steps used in their computation.

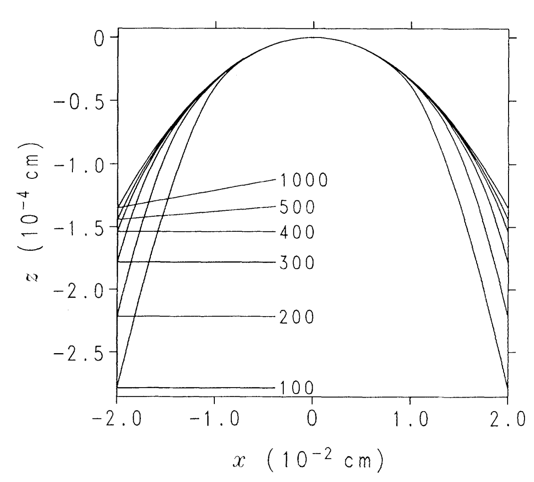

FIG. 4. Constant-phase surfaces corresponding to the intensities in Fig. 3 and labeled by the number of axial steps used in their computation.

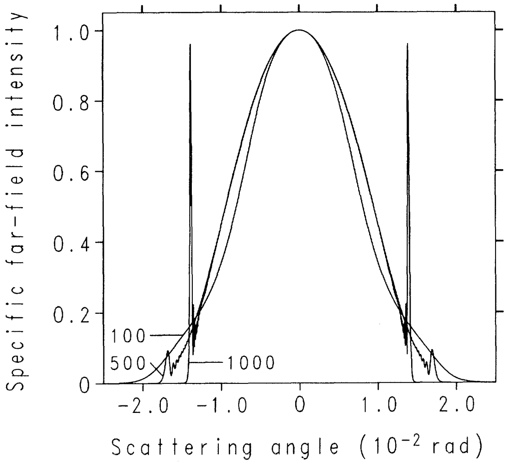

FIG. 5. Far-field angular distributions corresponding to the intensities in Fig. 3 and labeled by the number of axial steps used in their computation.

phase of a plane wave with wavelength $\lambda/\sqrt{\epsilon_a}$ [Eqs. (2) and (3)]. In paraxial calculations, the wavelength of the field remains very nearly equal to this wavelength. Consequently, the phase difference $[\phi(x,z)-\phi(0,z)]$ corresponds to an axial displacement $\lambda[\phi(x,z)-\phi(0,z)]/2\pi\sqrt{\epsilon_a}$. A very good approximation $Z(x)$ of a constant-phase surface passing through the z axis at z is thus

$$Z(x)=z-\frac{\lambda}{2\pi\sqrt{\epsilon_a}}[\phi(x,z)-\phi(0,z)] \ . \tag{137}$$

The 1000-step curve in Fig. 4 very closely exhibits the parabolic dependence

$$4-Z(x,4)=3.38\times10^{-1}x^2 \ , \tag{138}$$

so the phase has the parabolic form

$$\phi(x,4)=\phi(0,4)+1.06\times10^6x^2 \ . \tag{139}$$

The transverse wavelength $\lambda_t(x,z)$, decreasing as $\phi(x,4)$ increases quadratically, corresponds to a phase increase by 2π, i.e., $1.06\times10^6x^2+2\pi=1.06\times10^6[x+\lambda_t(x,4)]^2$, so

$$\begin{aligned}\lambda_t(x,4)&=-x+[x^2+2\pi/(1.06\times10^6)]^{1/2}\\&=\pi/(1.06\times10^6x)+\cdots \ ,\\x&>[2\pi/(1.06\times10^6)]^{1/2}=2.43\times10^{-3} \ .\end{aligned} \tag{140}$$

Since the uniform transverse zones have length 1.39×10^{-5} $(=8.015\times10^{-2}/5759)$, the on-axis wavelength is represented by 175 points $[\approx\lambda_t(0,4)/(1.39\times10^{-5})]$ while only 11 points $[\approx\lambda_t(0.02,4)/(1.39\times10^{-5})]$ resolve a transverse wave near the edge of the amplifier (Feit and Fleck [4] use about 5 points). The phase grows quadratically [Eq. (139)] only to the edge of the amplifier and then stays nearly constant because the free-electron density [Eq. (128)] extends no further. Thus $\lambda_t(0.02,4)$ $(=1.48\times10^{-4}$ cm) is the shortest transverse wavelength.

The parabolic dependence in Eqs. (138) and (139) is more or less to be expected. If there is no refraction or gain, i.e., only diffraction, Eqs. (60)–(63) show that the transverse phase varies as the product $x^2(z-z_0)$, where z_0 is the location of the beam waist. Similarly, if there is no diffraction (i.e., no Laplacian term) and no gain, Eq. (15) reduces to the steady-state form

$$\frac{\partial\mathcal{E}}{\partial z}=\frac{i\pi}{\lambda\sqrt{\epsilon_a}}[\epsilon(x)-\epsilon_a]\mathcal{E} \ , \tag{141}$$

which has the solution

$$\mathcal{E}(x,z)=\mathcal{E}(x,z_0)\exp\left\{\frac{i\pi}{\lambda\sqrt{\epsilon_a}}[\epsilon(x)-\epsilon_a](z-z_0)\right\} . \tag{142}$$

Equations (1), (128), (129), and (142) again indicate a transverse phase varying as $x^2(z-z_0)$. Gain affects mainly the amplitude of the field although saturation of the gain can also flatten the transverse variation. In any event, Fig. 4 illustrates that there is essentially an x^2 variation of the transverse phase when diffraction, refraction, and saturated gain are in effect simultaneously (the value of I_{sat} in Table I and the intensities of Fig. 3 imply that saturation is appreciable). Figure 6 illustrates how the transverse wavelengths decrease with axial propagation into the amplifier.

In summary, the transverse phase of the field increases approximately as the product $x^2(z-z_0)$ so, for a uniform grid, the number of grid points per transverse wave at the edge of the amplifier decreases inversely with the product $x(z-z_0)$. The shortest transverse wave with significant amplitude arises at the end of the amplifier and near its transverse edge. To provide some minimum number of grid points for this shortest wave, the number of points in a uniform grid must increase linearly with the length of the amplifier.

2. Discrete Fourier transforms, Hermitian-method finite differences, and Gauss-Hermite expansions

The foregoing DFT-FFT 1000-axial-step calculation can be done satisfactorily with a much sparser transverse grid. Figure 7 displays the near-field intensity computed with transverse grids of 5760, 1458, 1250, and 1176 points. Deterioration of the results becomes discernible with 1250 points. Significant distortion is apparent at 1176 points, which correspond to having only two points per shortest transverse wave [i.e., $\lambda_t(0.02,4)\times1175/0.08\approx2$]. Because of smaller truncation errors, these DFT-FFT results are superior to corresponding uniform-grid computations with the split-operator PIFD method (Sec. III). As Fig. 8 shows, the PIFD approach produces much larger sparse-grid distortions.

The advantage switches to the PIFD method when one admits nonuniform zoning, which, of course, is not an option with the DFT-FFT computations. Equation (140) indicates that the transverse wavelength decreases approximately linearly between the center of the amplifier

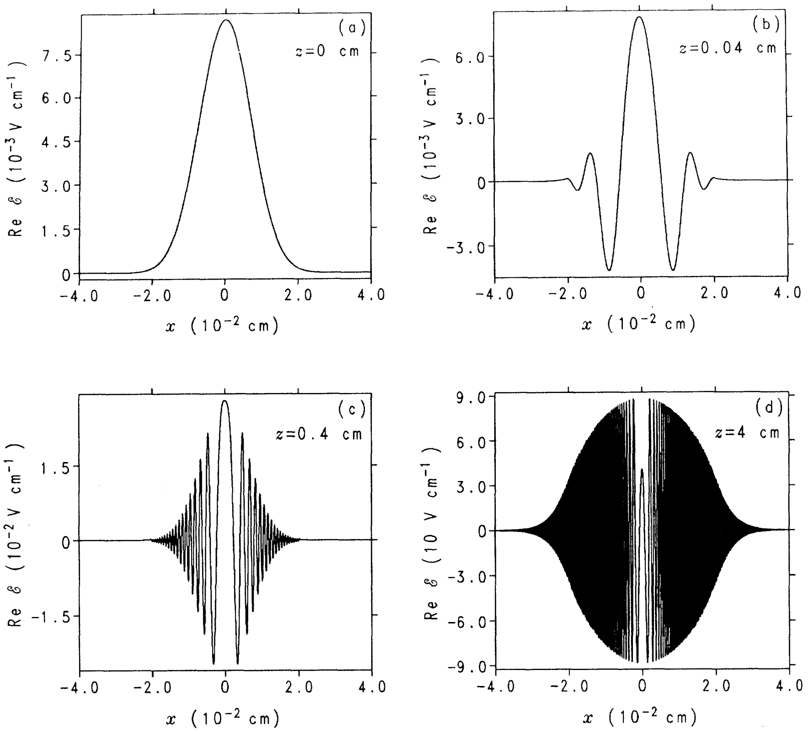

FIG. 6. Transverse profile of the real part of the field ℰ versus axial distance z.

and its edges (see also the near field at $z=4$ cm in Fig. 6), so one might expect the sparse-grid PIFD computations to improve if the density of the grid is adjusted in accord with this variation of the transverse wavelength. The uniform-grid size for $NX=1176$ in Fig. 8 is 6.896×10^{-5} $(=0.081\,03/1175)$. Consider a nonuniform grid in which (a) the interval $(-0.04,-0.03)$ is divided into 5 zones of length 2.000×10^{-3} $(=0.01/5)$; (b) the interval $(-0.03,0)$ is divided into 575 zones in such a way that the first zone has length 3.131×10^{-5} while each successive zone increases by 7.270×10^{-8} (an arithmetic series of intervals with increasing length) until the last zone has length

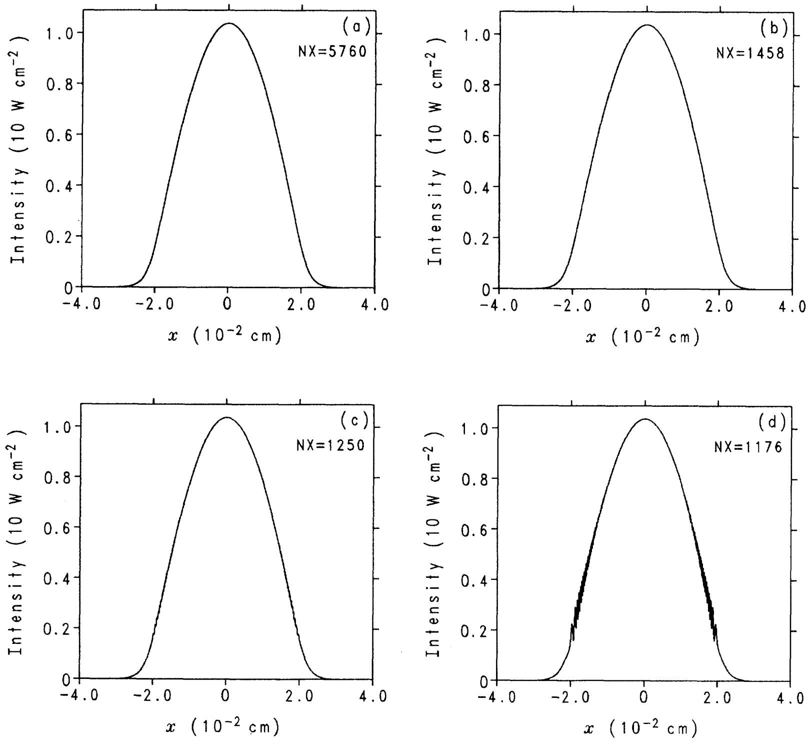

FIG. 7. DFT-FFT 1000-axial-step computation of near-field intensity vs NX, the number of points in the uniform transverse grid.

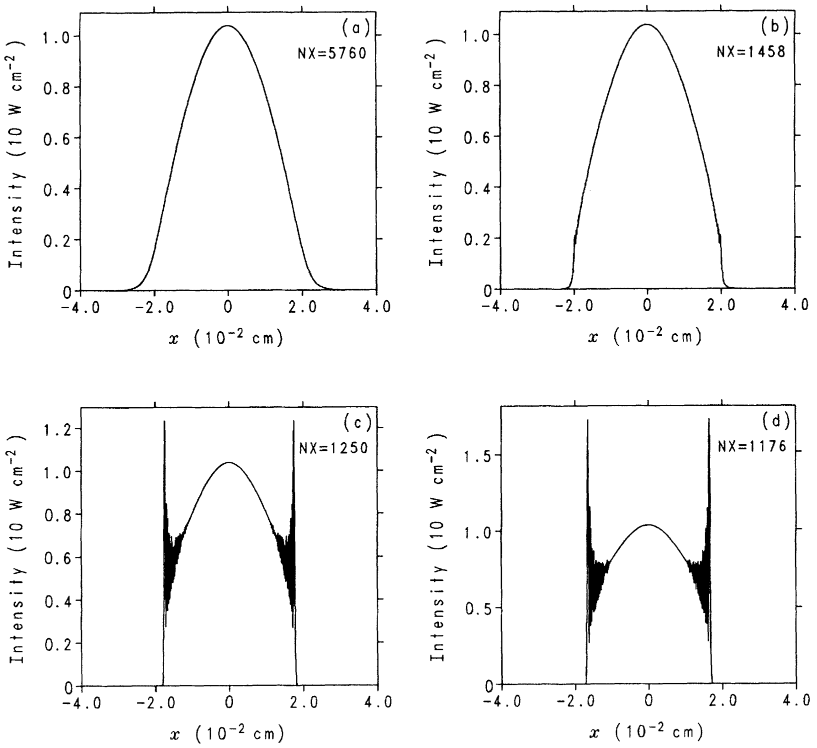

FIG. 8. PIFD 1000-axial-step computation of near-field intensity vs *NX*, the number of points in a uniform transverse grid.

7.304×10^{-5}; (c) the interval (0,0.03) is divided into 575 zones in such a way that the first zone has length 7.304×10^{-5} while each successive zone decreases by 7.270×10^{-8} (an arithmetic series of intervals with decreasing length) until the last zone has length 3.131×10^{-5}; (d) the interval (0.03,0.04103) is divided into 20 zones of length 5.515×10^{-4} (=0.01103/20). The PIFD curve in Fig. 9, obtained over this variable grid, is quite satisfactory and clearly superior to the DFT-FFT 1176-point results in Fig. 7.

Figure 10 illustrates three Gauss-Hermite expansions of the 5760-point curve in Fig. 8. The expansion with the spot-size parameter $\sigma_0=1.25\times10^{-3}$ cm, having a somewhat smaller breadth than the expansions for $\sigma_0=1.00\times10^{-3}$ or 1.50×10^{-3} cm, thereby reflects the optimal choice in Eq. (73). Figures 8 and 10 also demonstrate how even a relatively smooth near-field intensity can correspond to a very large Gauss-Hermite expansion. A Gauss-Hermite synthesis with the coefficients in Fig. 10 very closely reproduces the 1000-axial-step far-field curve in Fig. 5 and the 5760-point near-field curve in Fig. 7—the reproduction is so good that an overlay of the curves displays no discernible differences. A similar Gauss-Hermite synthesis with respect to the same transverse grid also yields the intermediate field at $z=5$ cm. This field, depicted in Fig. 11, extends beyond the boundaries of the transverse grid. To avoid distortions due to aliasing, such a computation via the DFT-FFT method requires that the field first be interpolated on a larger transverse grid.

If the 5760-point DFT-FFT distribution in Fig. 7 is uniformly rezoned onto the larger interval $(-5.000\times10^{-2},5.019\times10^{-2})$ via a monotone interpolation [15] of the real and imaginary parts of the field inside the initial interval $(-4.000\times10^{-2},4.015\times10^{-2})$, and via a zero-value extrapolation of the field outside the initial interval, a one-step DFT-FFT calculation yields Fig. 12, a noisy result that is clearly inferior to the Gauss-Hermite curve in Fig. 11. Distributing 7203 points uniformly over the interval $(-5.000\times10^{-2},5.019\times10^{-2})$, which yields the previous 5760 points over the smaller interval $(-4.000\times10^{-2},4.015\times10^{-2})$, produces, without rezoning, results that are indistinguishable from the

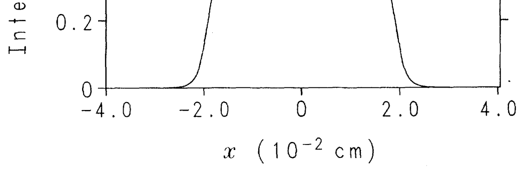

FIG. 9. PIFD 1000-axial-step computation of near-field intensity vs $NX=1176$, the number of points in a nonuniform transverse grid in which the density of zones is adjusted in accord with the near-field transverse wavelength given by Eq. (140) or Fig. 6.

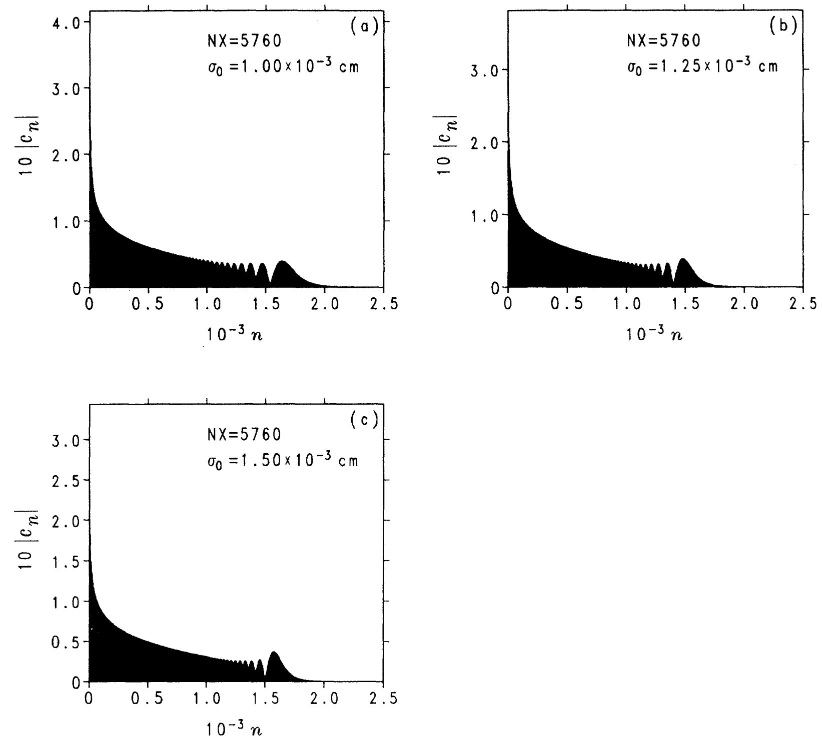

FIG. 10. Gauss-Hermite expansions of the 5760-point curve in Fig. 8 vs σ_0, the spot-size parameter in Eq. (63). These curves are constructed by straight-line interpolation. Because the coefficients of the expansions alternate between nonzero and zero values for even and odd modal indices, respectively, the drawings appear to be filled in solidly. The quantities n and $|c_n|$ are, respectively, the modal indices and coefficients of the series in Eq. (65).

5760-point curves in Figs. 7 and 11. But then the computational time very nearly equals that of the PIFD-Gauss-Hermite (PIFD-GH) approach. Table II summarizes the time data for Figs. 11 and 12.

Even though the arithmetic operations for one-step vacuum calculations via the PIFD and DFT-FFT methods vary, respectively, as N and $N \ln N$, where N is the dimension of the transverse grid; it turns out that the PIFD vacuum step requires nearly twice as much central-processor time as the DFT-FFT computation when N equals 5760 or 11 520, which lie in the range of the transverse dimensions needed for these calculations. Table III lists the computing times not only for the vacuum steps, but also for the amplitude-phase multipliers [Eqs. (22) and (23)] that complete the split-operator axial algorithms. Why the DFT-FFT amplitude-phase multiplier requires about 9% more time than the PIFD multiplier is puzzling since these calculations are theoretically identical. The difference between the DFT-FFT and PIFD vacuum steps narrows with the indicated doubling of the transverse dimension. Assuming computing times proportional to N and $N \ln N$, the aforementioned numbers of arithmetic operations, one infers from Table III that the DFT-FFT and PIFD vacuum steps would require the same computing time with a transverse dimen-

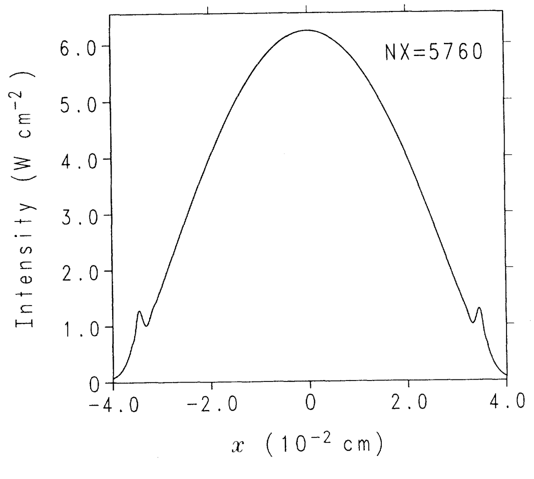

FIG. 11. Gauss-Hermite 5760-point synthesis of the field at $z = 5$ cm.

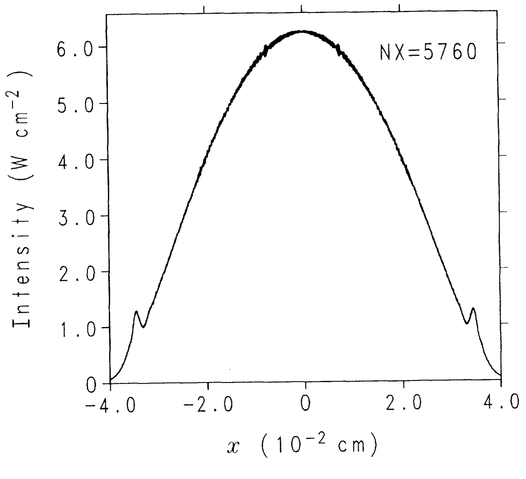

FIG. 12. DFT-FFT 5760-point calculation of the field at $z = 5$ cm. To avoid aliasing, the real and imaginary parts of the near field are uniformly and monotonely rezoned onto a larger transverse interval.

TABLE II. Central-processor timing (CRAY-Y/MP8) of DFT-FFT and PIFD-GH calculations for Figs. 11 and 12.

Calculation	5760-point PIFD-GH time (s)	5760-point DFT-FFT time (s)	7203-point DFT-FFT (s)
Inside laser	1.255×10^{2}	1.222×10^{2}	1.439×10^{2}
Vacuum step[a]	1.950×10^{1}	1.655×10^{-1}	4.000×10^{-2}
Total time	1.450×10^{2}	1.224×10^{2}	1.439×10^{2}

[a] The 5760-point DFT-FFT time includes the rezoning time.

sion of about 1.5×10^{7}. In other words, with any practical transverse dimension, the PIFD vacuum step needs about twice as much computing time as the DFT-FFT vacuum step. However, Table III also shows that the amplitude-phase multiplication requires 76–89 % of the entire calculation (i.e., vacuum step plus amplitude-phase multiplication), so these differences in computing times for the vacuum steps are relatively inconsequential.

A non-split-operator PIFD computation, performed in accord with Eq. (127), converges more slowly than the split-operator DFT-FFT (or PIFD) results in Figs. 3 and 4—about 4000 axial steps are needed to reach the degree of convergence exhibited by the 1000-step curves in these figures. Thus the elimination of operator splitting via Eq. (127), an option not available in the DFT-FFT approach, does not tip the scales in favor of the PIFD method inside the amplifier (cf. Scarmozzino and Osgood [19] and the discussion in Sec. III C 3). A numerical PIFD implementation, mentioned in connection with Eq. (127), may achieve more significant improvements like Scarmozzino and Osgood's results for simpler problems.

There is little practical difference between the DFT-FFT and PIFD approaches. Because the PIFD technique allows more flexible zoning and superior accuracy with specially tailored grids, I prefer it inside the amplifier. Outside the amplifier, the DFT-FFT one-step calculations, even with an interpolation onto a uniform transverse grid, are much more efficient than a Gauss-Hermite expansion. Moreover, for the more complicated fields encountered below in the simulation of spontaneous emission, it becomes practically impossible to obtain reasonably convergent and efficient Gauss-Hermite expansions. Consequently, the two-way results below are based on PIFD techniques inside the amplifiers, a monotone interpolation [15] onto a uniform grid when the internal grid is nonuniform, and one-step DFT-FFT calculations outside the amplifier.

3. *Cylindrical symmetry and Gauss-Laguerre expansions*

In some respects, a cylindrically symmetric analysis is more realistic than the foregoing slablike calculations. Consider an analog of the preceding considerations in which (a) the amplifier is described by an *rz* geometry and has no spontaneous emission; (b) the free-electron density, small-signal gain, and initial Gaussian beam are cylindrically symmetric analogs of the above slablike forms; (c) a radial grid uniformly covers the interval $(0,4.000\times10^{-2})$ with NR $(=2875)$ points, which correspond to the 5760 points distributed over the interval $(-4.000\times10^{-2},4.015\times10^{-2})$; and (d) the computations use the cylindrically symmetric PIFD method inside the laser and a Gauss-Laguerre expansion outside the laser (cf. Sec. III C 2). Figure 13 summarizes a PIFD 1000-axial-step computation of the near-field intensity, the near-field surface of constant phase, the Gauss-Laguerre expansion of the near field, and the far-field angular distribution. The intensity in Fig. 13 is about half of the 1000-axial-step curve in Fig. 3 while the corresponding phase surfaces in Figs. 4 and 13 are very nearly identical. The Gauss-Laguerre expansion coefficients span about half as many modes as their Gauss-Hermite analogs in Fig. 10 and also generate a much smoother curve since they do not alternate between nonzero and zero values, respectively, for even and odd modal indices. The Gauss-Laguerre coefficients, like their Gauss-Hermite analogs, also display an optimal spot-size parameter [Eq. (73)] near $\sigma_0=1.25\times10^{-3}$ cm. The far-field distribution again displays a local peak at about 1.38×10^{-2} rad, but its height is considerably less than its slablike analog in Fig. 5. Because the *r* grid has half as many zones as the preceding *x* grid, these cylindrical computations require about half as much computing time. The Gauss-Laguerre vacuum-step computation is reduced by anoth-

TABLE III. One-axial-step central-processor timing (CRAY-Y/MP8) of DFT-FFT and PIFD methods for transverse dimensions of 5760 and 11 520.

Calculation	DFT-FFT method (s)	PIFD method (s)
Vacuum step (5760)	1.353×10^{-2}	2.582×10^{-2}
Exponential amplitude-phase multiplication (5760)	1.088×10^{-1}	9.979×10^{-2}
Vacuum step (11 520)	2.785×10^{-2}	5.150×10^{-2}
Exponential amplitude-phase multiplication (11 520)	1.741×10^{-1}	1.601×10^{-1}

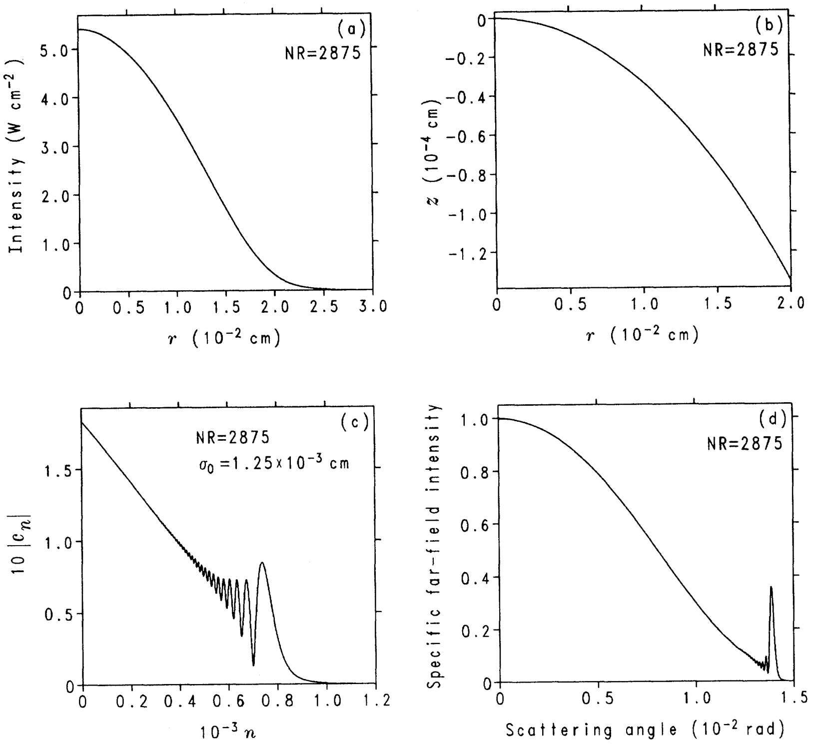

FIG. 13. Cylindrically symmetric PIFD 1000-axial-step computation: (a) near-field intensity, (b) near-field surface of constant phase, (c) Gauss-Laguerre expansion of the near field [n and $|c_n|$ are, respectively, the modal indices and coefficients of the series in Eq. (80)], (d) far-field angular distribution.

er factor of $\frac{1}{2}$ since its coefficients span about half as many modal indices.

4. Refraction and gain computed separately

It is interesting to examine the effects of refraction and gain separately. Figure 14 displays a DFT-FFT 1000-axial-step computation with 7203 points distributed over the interval $(-5.000\times10^{-2},5.019\times10^{-2})$. The small-signal gain is zero while the preceding parabolic free-electron density is retained. The far-field distribution has even more prominent peaks at 1.38×10^{-2} rad because its central portion is no longer amplified. The intricate interference pattern, smeared together by the coarse scale of the drawing, is well resolved by the 7203-point grid.

If the roles of the density and gain are reversed (i.e., use the preceding parabolic small-signal gain and zero density), one obtains the much narrower and smoother outer curve in Fig. 15. This zero-density distribution has barely discernible peaks in its wings at about 1.6×10^{-4} rad. The inner curve in Fig. 15 is the Gaussian-beam distribution for vacuum transport, so the saturated gain produces a relatively small extra spreading. Consequently, refraction due to the nonuniform density—and not slightly greater gain along certain curved rays—causes the prominent maxima in the wings of the far-field distribution.

5. Discretization, underestimated diffraction, and overestimated power output

When the spontaneous emission is modeled in accordance with Eq. (130) and the accompanying commentary, each emissive injection has the same smooth profile of intensity. However, each realization of the phase differs and has an arbitrarily high "mode content"—the longer is the sequence of pseudorandom numbers used to generate the random phase, the greater is the spread of modes in the distribution. Since the dimension of the transverse grid must increase in concert with the length of this sequence, the modal content of this modeling is strictly limited.

What is an adequate modal content? As it increases, the output of the laser decreases more or less steadily as more and more radiation diffracts laterally and hence

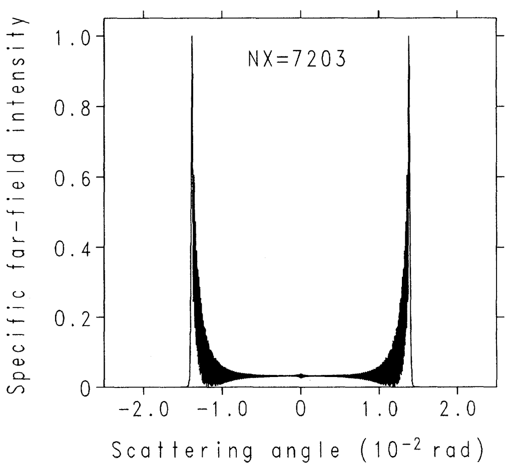

FIG. 14. DFT-FFT 1000-axial-step 7203-point calculation of far-field angular distribution for parabolic density and zero gain.

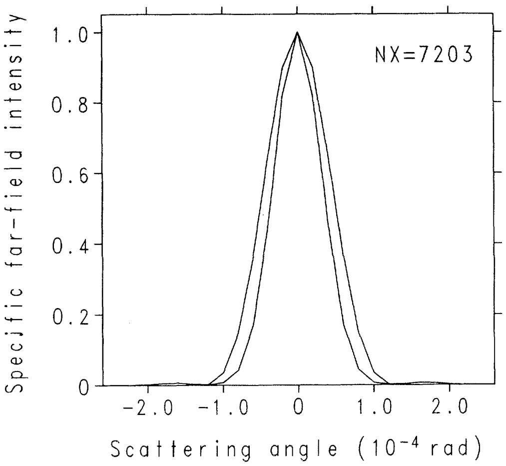

FIG. 15. DFT-FFT 1000-axial-step 7203-point calculation of far-field angular distribution (outer curve) for parabolic gain and zero density. The outer curve has the barely discernible peaks at 1.6×10^{-4} rad. The inner curve is the Gaussian-beam distribution for vacuum transport.

does not undergo full amplification. For a laser of length l and width w, the far-field radiation would be confined approximately within an angle w/l $(=1.0\times10^{-2})$ if there were no diffraction or refraction. However, Figs. 5, 13, and 14 show that even a simple Gaussian beam exceeds such an angular divergence, i.e., the refraction by itself directs radiation somewhat outside the geometric-optics limits of the laser. It seems reasonable to use a modal distribution extending up to where the diffraction spreading rivals this refractive divergence. All modes receiving full amplification are included, and adequate statistics for coherence calculations should be realized. Such a procedure obviously underestimates the total diffraction and thereby overestimates the power output.

Present supercomputer storage and speed are very many orders of magnitude less than what would be required to model the full modal content of real x-ray lasers. If a calculation is to yield an observed power output, the constant A in Eq. (130) must be adjusted. Even a specification of A based on detailed microscopic modeling will result in too little diffraction and too much power.

To estimate a modal distribution for which the diffractive spreading is about the same as that of the refraction, consider a computational experiment in which (a) the emissive injections use the model in Eq. (130); (b) these injections are separated by 0.1 cm (i.e., there are 41 injections in each calculation); (c) the DFT-FFT method is used over the transverse interval $(-6.000\times10^{-2}, 6.340\times10^{-2})$, which is large enough to avoid aliasing; (d) there is no refraction (i.e., only diffraction and saturated gain are in effect); (e) a series of calculations incorporates successively longer sequences of pseudorandom numbers to generate the random phases of the emission; (f) the number of points in the transverse and axial grids increases appropriately with the increasing phase complexity to ensure well-converged and well-resolved results; (g) the near field, the power, and the far-field angular distribution are monitored.

Figure 16(a) illustrates the common emissive profile of intensity. A typical phase-curve realization for 151 random points interpolated by 1401 x-grid points is

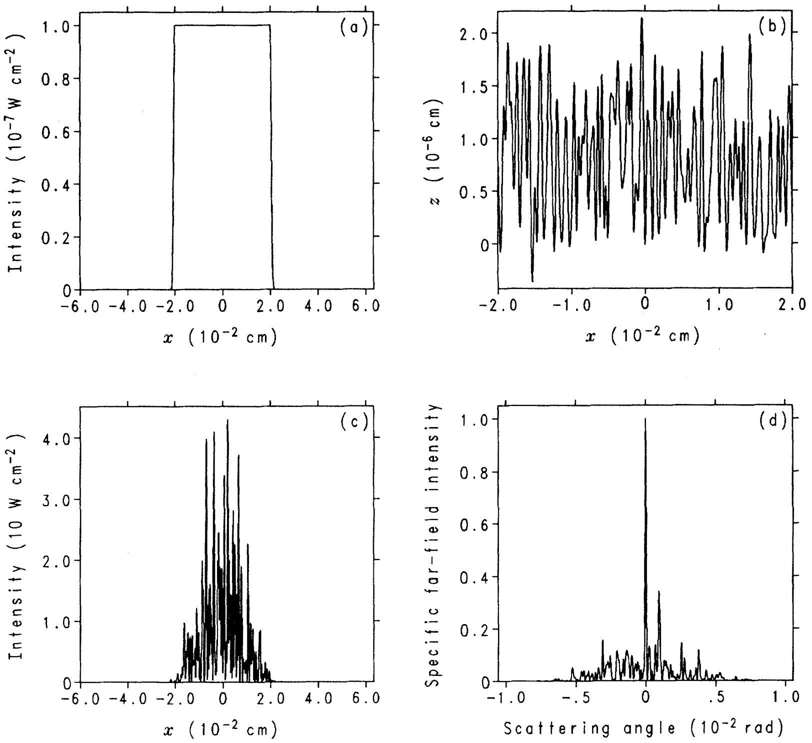

FIG. 16. Computation with 151-point random-phase sequences: (a) profile of emissive intensity injected at intervals of 0.1 cm, (b) typical random-phase curve, (c) near-field intensity, (d) far-field angular distribution. The near-field power density (total power per unit distance perpendicular to the intensity plot) is 2.873×10^{-1} W cm^{-1}.

displayed in Fig. 16(b). Figures 16(c) and 16(d) show, respectively, the near-field intensity and the far-field distribution. The near field spills slightly outside the transverse boundaries of the laser, and the angular spread ($\approx 8.0\times10^{-3}$ rad) of the far field is approaching the geometric-optics limits ($=1.0\times10^{-2}$ rad) of the laser.

Table IV summarizes the results of a family of such calculations. The angular divergence increases until the geometric-optics limit is attained at about 201 random points while the total power fluctuates with increasing phase complexity until it starts to drop off as significantly greater amounts of radiation diffract laterally and thereby receive less than the full amplification available. Even with one-way computation, following this process of diminishing output demands formidable zoning dimensions; and the goal is to perform two-way computations. One would hope that about 151 random points lead to adequate statistics for coherence calculations.

6. *Single-mode-like evolution, refraction, and saturation of the gain*

Refraction enhances the evolution of a single-mode-like intensity whereas saturation of the gain inhibits this process. The word "single-mode-like" has to be emphasized because, even though the intensity can have a very simple profile like a low-order Gauss-Hermite mode, the phase surface may differ greatly from such a mode and thereby lead to a very large Gauss-Hermite expansion—see Figs. 6 and 10.

Consider again the emission depicted by Figs. 16(a) and 16(b), and suppose that this emission is injected only at the input of the laser. Cover the transverse interval $(-6.000\times10^{-2}, 6.340\times10^{-2})$ with a uniform grid of 4320 points, and use 1200 uniform axial points to transport this emission over the length of the laser. Figures 17(a) and 17(b) depict, respectively, the 1-pass and 2-pass outputs of a DFT-FFT computation in which (a) there is no refraction and (b) the preceding parabolic small-signal gain is unsaturated (i.e., $I_{\text{sat}}=1.000\times10^{100}$ W cm^{-2}). Figures 17(c) and 17(d) display the same 1-pass and 2-pass results when refraction via the foregoing parabolic charge density is in effect. Refraction clearly produces the more rapid evolution of a single-mode-like intensity.

Figure 18 redoes the calculations in Fig. 17 with a saturated gain (I_{sat} has the value in Table I). The transverse grid for Figs. 18(c) and 18(d) is augmented to 6400 points distributed uniformly over the interval $(-9.000\times10^{-2}, 9.283\times10^{-2})$ in order to avoid too much aliasing. That saturation of the gain reduces the rate of single-mode-like evolution is evident from a comparison of Figs. 18(a), 18(b), 18(c), and 18(d) with Figs. 17(a), 17(b), 17(c), and 17(d), respectively.

Multi-mode-like behavior is still present after two passes. Since the laser may deteriorate significantly by the end of the second pass, some sort of modal filtering or an unstable-resonator mirror may be needed to facilitate the evolution of a satisfactory 2-pass output.

7. *Near-field and far-field sensitivity to charge density and small-signal gain*

Because its slope does not possess an unphysical discontinuity at the edge of the laser, the Gaussian profile [Eq. (129)] may provide more realistic results. Reconsider the DFT-FFT 1000-axial-step 7203-transverse-point calculation for Fig. 14, assume there is no gain, and let the charge density have the Gaussian profile of Eq. (129). Figure 19(a) shows the corresponding near-field output, which displays none of the intricate interference in Fig. 14. Moreover, this near field has an on-axis dip similar to previous results [3,4] connected with a quartic profile for the small-signal gain. An additional unsaturated gain, extending flatly and more widely than the distribution in Fig. 19(a), would produce a similar result.

If a Gaussian small-signal gain like Eq. (129) is added to the computation behind Fig. 19(a), one obtains the far-field distribution in Fig. 19(b), which differs remarkably from Fig. 14. There are no spikes or intricate interference, while the flattening influence of saturated gain is evident and produces output that is quite uniform within the geometric-optics limits ($=1.0\times10^{-2}$ rad) of the laser.

If the profiles for density and gain are interchanged in the calculation leading to Fig. 19(a) (i.e., a Gaussian gain and zero density), the very different and relatively narrow

TABLE IV. Near-field power density and far-field angular divergence versus dimension of random-phase sequence.

Random-phase dimension	NX[a]	NZ[b]	Near-field power density[c] (W cm^{-1})	Far-field angular divergence (rad)
21	640	400	3.085×10^{-1}	1.6×10^{-3}
101	4 320	800	3.051×10^{-1}	6.0×10^{-3}
151	4 320	1 200	2.873×10^{-1}	8.0×10^{-3}
201	6 040	1 600	3.094×10^{-1}	9.0×10^{-3}
401	12 005	8 000	2.798×10^{-1}	1.0×10^{-2}
601	18 144	16 000	2.574×10^{-1}	1.0×10^{-2}
801	24 010	24 000	2.481×10^{-1}	1.0×10^{-2}

[a] NX is the x-grid dimension.

[b] NZ is the number of z steps in the calculation.

[c] The power density along the slab (i.e., along the y axis) is computed by using piecewise parabolic interpolation to evaluate the x integral of the near-field intensity.

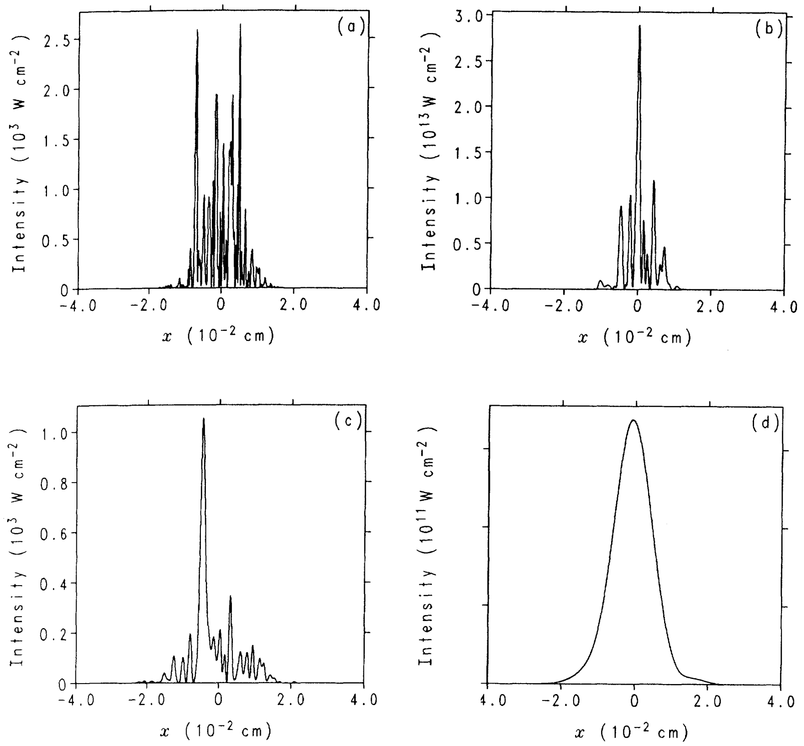

FIG. 17. DFT-FFT 1200-axial-step 4320-point near-field calculations with an unsaturated parabolic small-signal gain: (a) one pass with no refraction, (b) two passes with no refraction, (c) one pass with refraction via a parabolic charge density, (d) two passes with refraction via a parabolic charge density.

Gaussian-like intensity in Fig. 19(c) ensues. Adding a Gaussian density to this calculation generates refraction and thereby produces the wider near-field Gaussian-like intensity in Fig. 19(d).

Thus, Figs. 3, 5, 14, 15, and 19 demonstrate that both the near field and the far field are sensitive to the profiles of charge density and gain. Detailed hydrodynamics and atomic kinetics are essential for an accurate simulation of the output of an x-ray laser.

B. Two-way calculations

Much more involved computation becomes necessary when an accurate simulation of two-way saturated gain is

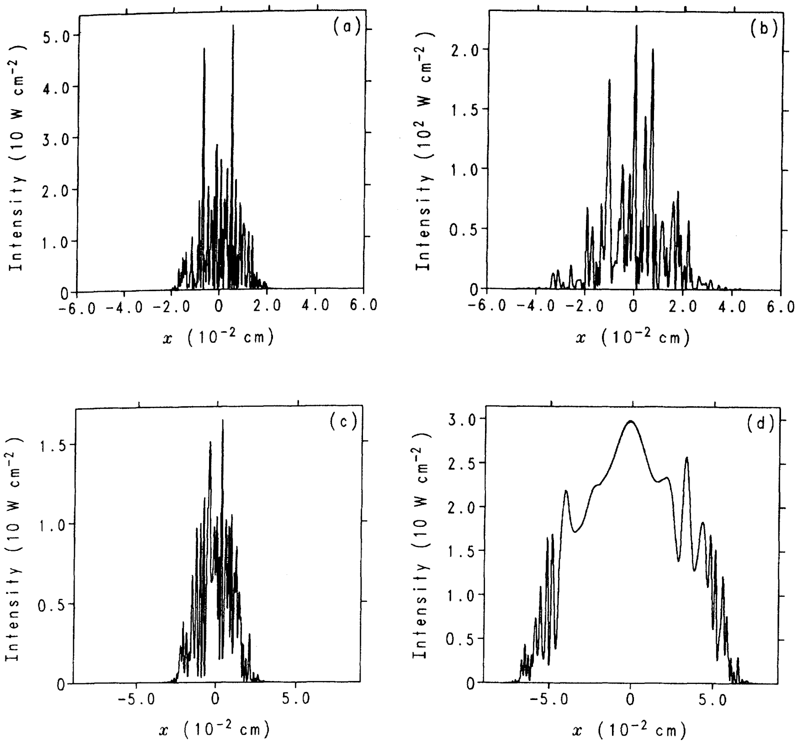

FIG. 18. DFT-FFT 1200-axial-step 6400-point near-field calculations with a saturated parabolic small-signal gain: (a) one pass with no refraction, (b) two passes with no refraction, (c) one pass with refraction via a parabolic charge density, (d) two passes with refraction via a parabolic charge density.

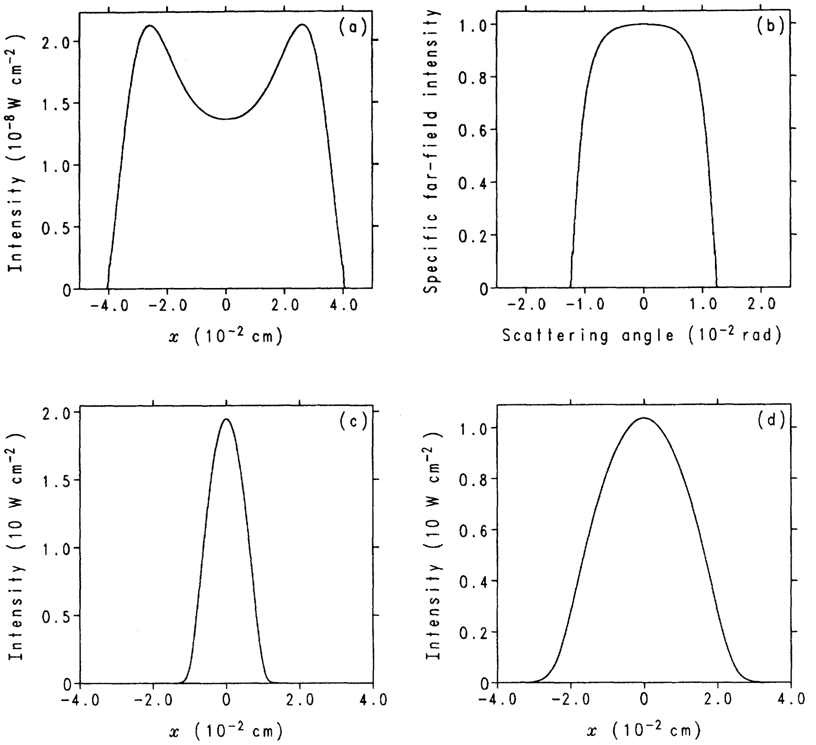

FIG. 19. DFT-FFT 1000-axial-step 7203-point calculations: (a) near-field intensity with Gaussian charge density and no gain, (b) far-field distribution with Gaussian charge density and Gaussian small-signal gain, (c) near-field intensity with no refraction and Gaussian small-signal gain, (d) near-field intensity with Gaussian charge density and Gaussian small-signal gain.

desired. In all that follows, the charge density and small-signal gain have the parabolic forms defined by Eq. (128) and the related data in Table I.

1. *Parametric adjustment to previous work*

Consider the following nonuniform transverse grid for the two-way PIFD calculations inside the amplifier: (a) the interval $(-0.6,-0.06)$ is covered by 100 arithmetic-series decreasing-length zones, ending with the common length of the zones in the next interval; (b) the interval $(-0.06,0.06)$ is uniformly divided into 4200 zones; and (c) the interval $(0.06,0.6)$ is covered by 100 arithmetic-series increasing-length zones, starting with the common length of the zones in the preceding interval. For the one-way DFT-FFT calculations outside the laser, use a uniform transverse grid of 4320 points over the interval $(-0.06,0.0634)$ and map the nonuniform-grid data onto this uniform grid via monotone amplitude-phase interpolation [16]. Also, let the spontaneous-emission injections be similar to the sample illustrated by Figs. 16(a) and 16(b), but reduced somewhat in modal content to 141 random-phase points, which barely generate enough diffractive spreading to rival the refractive spreading.

This grid and the values of A and I_{sat} in Table I are compatible with Feit and Fleck's simulations [4]. For example, perform a 100-axial-cell 500-axial-step 3-cycle 5-pass computation [$M=5$ and $N=100$ in Eq. (50), three shooting-secant iterations are executed for each axial-temporal step across each axial cell, and the computation transports light through 5 lengths of the laser]. Figure 20 displays the instantaneous axial variation of the saturated gain, transversely averaged over the width of the laser. Although less peaked near the middle of the laser, the curve in Fig. 20 is quite similar to Feit and Fleck's Fig. 4, reaching a gain of about 4 cm^{-1} in the middle of the laser and dropping more or less symmetrically to about 1.6 cm^{-1} at its ends.

2. *Mostly noniterative computation*

Figures 21(a) and 21(b) show, respectively, the time-averaged near-field and the time-averaged far-field distribution from a noniterative 100-axial-step 5-pass calcula-

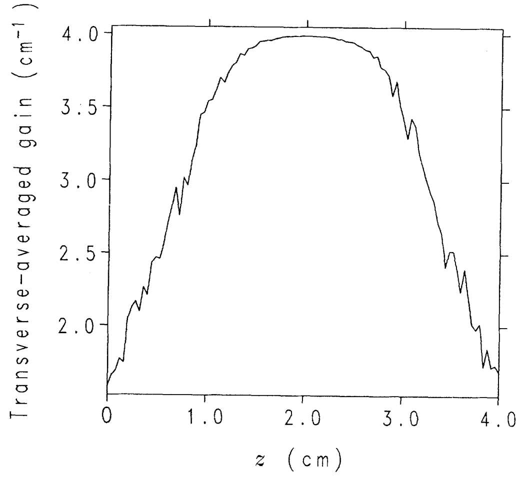

FIG. 20. 100-axial-cell 500-axial-step 3-cycle 5-pass computation of the axial variation of the saturated gain, transversely averaged over the width of the amplifier.

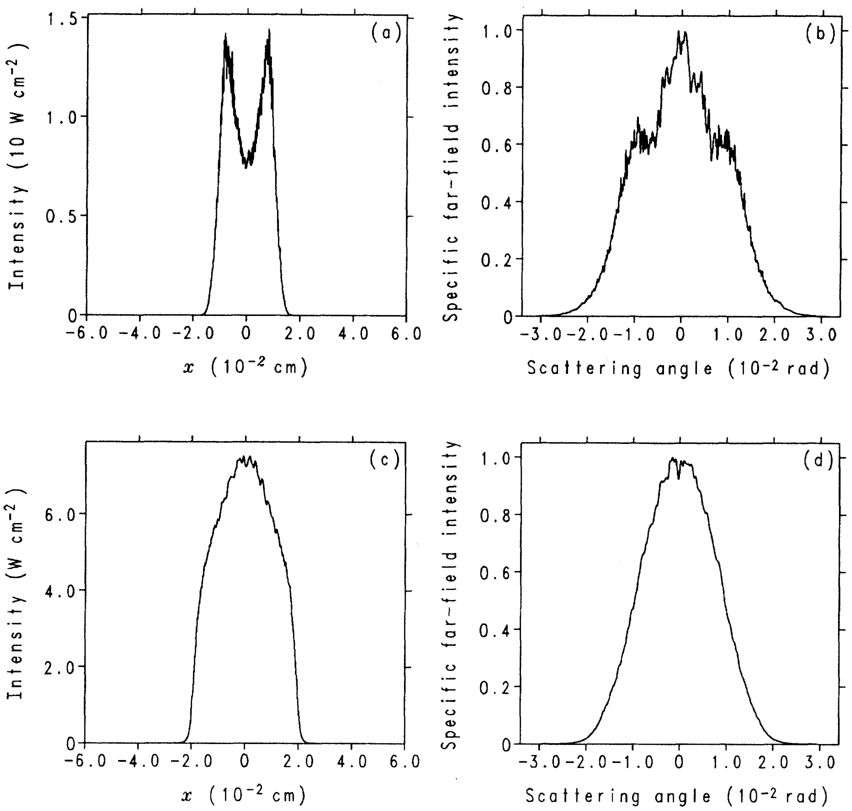

FIG. 21. Noniterative 5-pass time-averaged calculations: (a) 100-axial-step near-field intensity, (b) 100-axial-step far-field distribution, (c) 500-axial-step near-field intensity, (d) 500-axial-step far-field distribution.

tion, which gives 500 samples for the time averages. Figures 21(c) and 21(d) result when the axial resolution of this calculation is increased to 500 steps, which yield 2500 samples for the time averaging. In accordance with the random-walk linear-gain relations in Eqs. (131)–(135), the amplitude A in Table I is reduced to 4.069×10^{-3} V cm^{-1}. Figures 21(a) and 21(c) have the same qualitative relationship as the 100-step and 500-step one-way curves in Fig. 3—very distorted results are obtained with only 100 steps. Several curves in [4] have the same broad two-pronged shape as Fig. 21(a) and thus represent, I submit, very unconverged calculations.

The array storage and computing time for the calculation behind Figs. 21(a) and 21(b) are, respectively, 1 892 510 (decimal) 64-bit words and 17.4 min per pass on a Cray-Y/MP8 machine. The corresponding storage and time for Figs. 21(c) and 21(d) are, respectively, 8 934 510 and 430.5 min per pass, so properly converged noniterative calculations can tax supercomputers. Comparisons between Figs. 21(a) and 21(c), and between Figs. 21(b) and 21(d), indicate that the 100-axial-step calculation produces a too narrow near field and an overly wide far-field distribution.

The spatial-coherence curves [Eq. (136)] corresponding to Figs. 21(a) and 21(c) are plotted, respectively, in Figs. 22(a) and 22(b)—the laser is not very coherent. The wings of Fig. 22(b), based on 5 times as many time samples, are considerably smaller and less noisy than the wings of Fig. 22(a). This pattern is common with coherence calculations. The central portion of a coherence curve emerges with a relatively few time samples, but the amplitude and noise of the wings disappear relatively slowly as the number of time samples grows. The wings of the coherence curves in [4] are not nearly as noisy because, unlike Figs. 22(a) or 22(b), Feit and Fleck's results appear not to be plotted at the full density of the transverse grid.

In order to assess the accuracy of Figs. 22(a) and 22(b), consider the more refined calculation in Fig. 22(c). The number of transverse zones inside the interval $(-0.06,0.06)$ is increased to 9000, the rest of the grid is unchanged, the number of random-phase points increases to 301, and the number of axial steps is doubled via a 10-axial-cell 1000-axial-step 3-cycle 5-pass computation [$M=100$ and $N=10$ in Eq. (50), the time averages are based upon 50 time samples, and the amplitude A in Table I is increased to 1.792×10^{-2} V cm^{-1} in accord with Eqs. (131)–(135)]. With only 50 time samples, the wings of the coherence curve have greater amplitudes, but the width of the central portion of this curve is substantially narrower. Figure 22(d) overlaps the central parts of the curves in Figs. 22(a)–22(c) and labels each curve by the number of time samples used for its computation. The coherence calculations in Figs. 22(a) and 22(b) are clearly optimistic.

3. *Iterative computation*

Although the computation for Figs. 21(c) and 21(d) provides fairly well-converged results, the storage and computing time are prohibitive, especially if one contemplates an integration with hydrodynamics and detailed

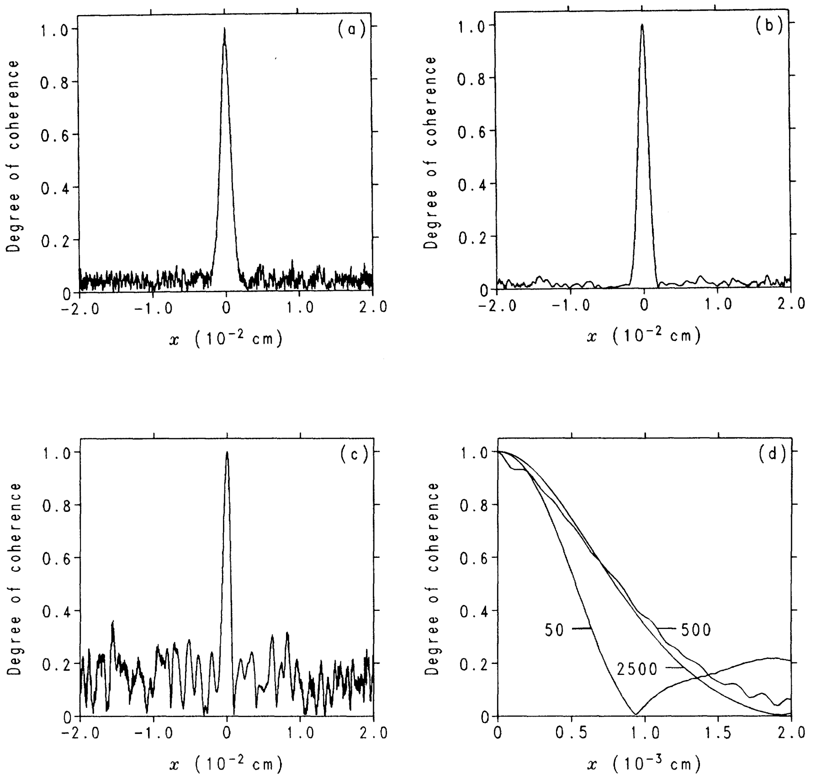

FIG. 22. Spatial-coherence curves [moduli of complex coherence factor defined by Eq. (136)]: (a) curve corresponding to Fig. 21(a); (b) curve corresponding to Fig. 21(c); (c) more refined curve resulting from 301 random-phase points, 9000 transverse points, and a 10-cell 1000-axial-step 3-cycle 5-pass computation; (d) an overlay of the central parts of the curves in Figs. 22(a)–22(c), labeled by the number of time samples used in their calculation.

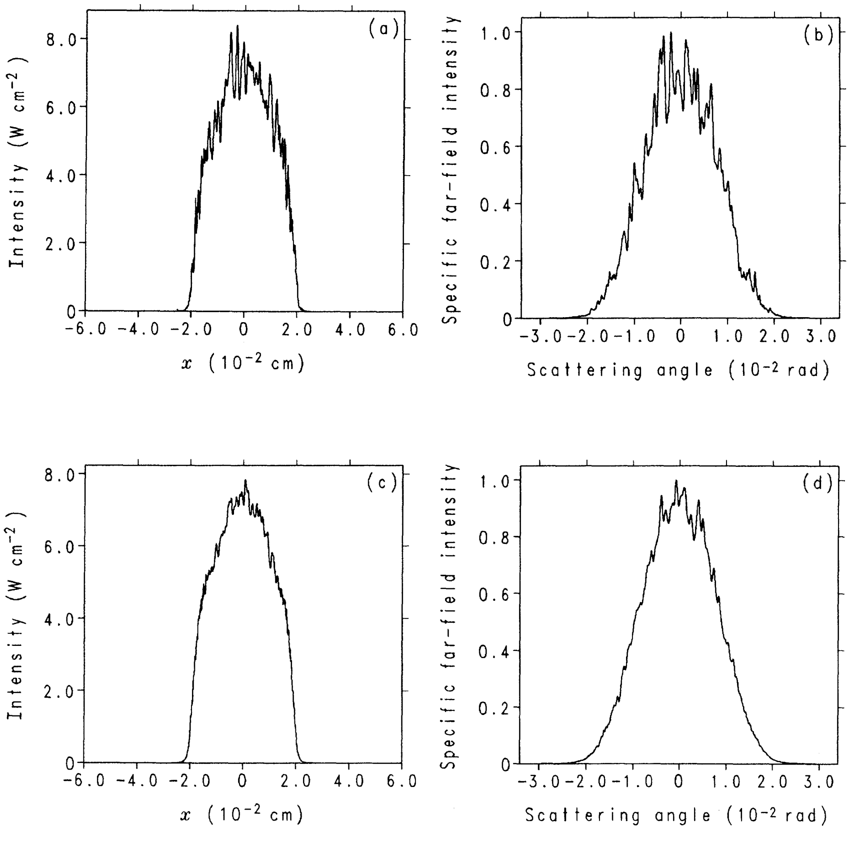

FIG. 23. Iterative 500-axial-step 3-cycle 5-pass time-averaged calculations: (a) 10-axial-cell near-field intensity, (b) 10-axial-cell far-field distribution, (c) 100-axial-cell near-field intensity, (d) 100-axial-cell far-field distribution.

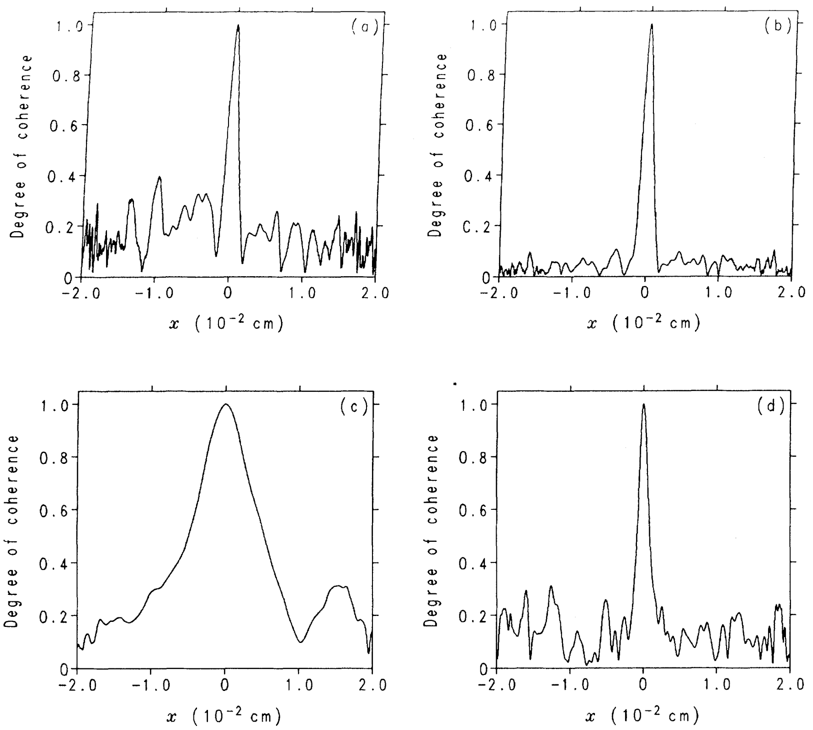

FIG. 24. Spatial-coherence curves [moduli of complex coherence factor defined by Eq. (136)]: (a) curve corresponding to Fig. 23(a), (b) curve corresponding to Fig. 23(c), (c) curve corresponding to Fig. 24(a) when the number of random-phase points is reduced from 141 to 21, (d) curve corresponding to Fig. 24(c) when the calculation is redone with no refraction.

atomic kinetics. Moreover, the one-way calculations in Figs. 3–5 indicate that more axial steps are desirable. Iterative computation allows more axial resolution with less computing time and greatly reduced storage.

Figures 23(a) and 23(b) display the near field and the far field for a 10-axial-cell 500-axial-step 3-cycle 5-pass calculation over the same transverse grid. The storage and time are, respectively, only 352 070 and 28.3 min per pass. Figures 23(a) and 23(b) agree remarkably well with Figs. 21(c) and 21(d). Of course, Figs. 23(a) and 23(b) are noisier because their time averages are based on only 50 samples instead of 2500 samples. The intermediately noisy 500-time-sample curves in Figs. 23(c) and 23(d) derive from the calculation for Fig. 20. It uses a storage of 1 936 520 and a time of 292.5 min per pass. The 50-time-sample calculation for Fig. 23(a) and the 500-time-sample calculation for Fig. 23(c) provide, respectively, the coherence curves in Figs. 24(a) and 24(b). Figures 22(b), 24(a), and 24(b) have virtually the same central portion, so the relatively few time samples available in an iterative calculation do not constitute a significant disadvantage for the computation of coherence curves. Table V summarizes the convergence, efficiency, storage, and time step of the foregoing iterative and noniterative com-

TABLE V. Convergence, storage, efficiency, and time step of various iterative and noniterative two-way computing strategies.

Strategy	Converged?	Storage[a]	Cray-Y/MP8 time per pass[b] (min)	Time step[c]
100-axial-step, noniterative[d]	No	1 892 510	17.4	$l\sqrt{\epsilon_a}/100c$
500-axial-step, noniterative	Yes[e]	8 934 510	430.5	$l\sqrt{\epsilon_a}/500c$
500-axial-step, 10-cell, 3-cycle, iterative	Yes[e]	352 070	28.3	$l\sqrt{\epsilon_a}/10c$
500-axial-step, 100-cell, 3-cycle, iterative	Yes[e]	1 936 520	292.5	$l\sqrt{\epsilon_a}/100c$

[a] The total array storage in a calculation is listed as a decimal number of 64-bit words.

[b] One pass means that the calculation transports light through one length of the amplifier.

[c] The parameters c, l, and ϵ_a are, respectively, the velocity of light in vacuum, the length of the amplifier, and the space-time average of the dielectric constant [Eq. (2)].

[d] This is the basic calculation in Feit and Fleck [4].

[e] The convergence would be perceptibly better with 1000 axial steps (cf. Figs. 3 and 4).

puting strategies.

The much wider coherence curve in Fig. 24(c) results when the number of random-phase points underlying Fig. 24(a) is reduced from 141 to 21. Thus, as one expects, the coherence of the amplifier increases as the modal content diminishes. When the calculation behind Fig. 24(c) is redone with no refraction (e.g., a uniform charge density), one obtains the much narrower curve in Fig. 24(d). Refraction therefore improves spatial coherence even though it leads to many more transverse modes connected with a highly curved phase surface (cf. Secs. IV A 1 and IV A 2) and intricate interference at the edges of the amplifier (cf. Sec. IV A 4).

V. CONCLUDING REMARKS

My primary message is that two-way paraxial wave-optics simulations of x-ray lasers need not consume all the resources of a supercomputer. One does not have to accept calculations [4] that require at least five times more points to yield only modestly converged results. Because the near field and far field are so sensitive to the profiles of the charge density and the small-signal gain, serious modeling should include hydrodynamics and adequately detailed atomic kinetics. Presently conceived amplifiers probably do not attain stationary operation so serious evaluations of coherence should be nonstationary (i.e., ensemble averaged instead of time averaged). Such computing refinements, which are accessible with present hardware and the shooting-secant iterations outlined in this paper, could help to optimize x-ray lasers.

Several techniques, not considered herein, could improve the computations in question. Significant enhancement of speed and/or accuracy may be possible with parallel computation—the shooting-secant iterations are intrinsically parallelizable. The numerical implementation of the integral Hermitian method applied to the nonsplitting of operators (Sec. III C 3) may also yield significant improvement. Third-order expansion of the diagonal exponential multipliers (Sec. III C 3) helps when the axial steps are sufficiently small. Just as the fast-Fourier-transform approach is, in most cases, superior to Gauss-Hermite expansions (Sec. IV A 2), a fast-Hankel-transform algorithm may be mostly superior to Gauss-Laguerre expansions in cylindrically symmetric calculations (Sec. IV A 3). Therefore, the performance of the various fast-Hankel-transform algorithms should be checked.

ACKNOWLEDGMENTS

I am especially grateful for S. Dalhed's support of an extensive effort. Many conversations with J. A. Viecelli, C. H. Woods, and G. W. Hedstrom were very helpful. Because of budgetary constraints, this work was completed without direct sponsorship—a circumstance graciously accommodated by C. K. Westbrook. This work was performed under the auspices of the U.S. Department of Energy by the Lawrence Livermore National Laboratory under Contract No. W-7405-ENG-48.

---

[1] C. H. Skinner, Phys. Fluids B **3**, 2420 (1991).
[2] Lawrence Livermore National Laboratory Report No. CONF-9206170, 1992 (unpublished).
[3] R. A. London, Phys. Fluids **31**, 184 (1988).
[4] M. D. Feit and J. A. Fleck, Jr., J. Opt. Soc. Am. B **7**, 2048 (1990).
[5] J. C. Garrison, B. Ritchie, H. Nathel, C. K. Hong, and L. Minner, Phys. Rev. A **43**, 4941 (1991).
[6] P. R. Garabedian, *Partial Differential Equations* (Wiley, New York, 1964), Chap. 2.
[7] R. A. London, P. Amendt, M. Strauss, M. D. Rosen, M. D. Feit, and J. A. Fleck, Jr., in *X-Ray Lasers 1990*, edited by G. J. Tallents (Hilger, Bristol, 1991), p. 363.
[8] J. D. Jackson, *Classical Electrodynamics*, 2nd ed. (Wiley, New York, 1975), p. 288.
[9] J. L. Walsh and P. B. Ulrich, in *Laser Beam Propagation in the Atmosphere*, edited by J. W. Strohbehn (Springer-Verlag, New York, 1978), Sec. 7.2.1.
[10] A. E. Siegman, *Lasers* (University Science, Mill Valley, CA, 1986), p. 207.
[11] R. Courant and D. Hilbert, *Methods of Mathematical Physics* (Interscience, New York, 1953), Vol. I, p. 140.
[12] J. A. Fleck, Jr., J. R. Morris, and M. D. Feit, Appl. Phys. **10**, 129 (1976).
[13] H. Kogelnik and T. Li, Proc. IEEE, **54**, 1312 (1966).
[14] A. E. Siegman, *Lasers* (Ref. [10]), p. 691.
[15] F. N. Fritsch and R. E. Carlson, SIAM J. Numer. Anal. **17**, 238 (1980).
[16] M. D. Feit and J. A. Fleck, Jr., Opt. Lett. **14**, 662 (1989).
[17] L. Collatz, *The Numerical Treatment of Differential Equations*, 3rd ed. (Springer-Verlag, New York, 1960), Chap. III.
[18] M. E. Rose, Math. Comput. **18**, 179 (1964).
[19] R. Scarmozzino and R. M. Osgood, Jr., J. Opt. Soc. Am. A **8**, 724 (1991).
[20] J. A. Fleck, Jr., J. Comput. Phys. **16**, 324 (1974).
[21] M. Born and E. Wolf, *Principles of Optics*, 6th ed. (Pergamon, New York, 1985), Chap. X.
[22] J. W. Goodman, *Statistical Optics* (Wiley, New York, 1985), Chap. 5.
[23] R. A. London, M. Strauss, and M. D. Rosen, Phys. Rev. Lett. **65**, 563 (1990).
[24] P. Amendt, R. A. London, and M. Strauss, Phys. Rev. A **44**, 7478 (1991).
[25] M. D. Feit and J. A. Fleck, Jr., Opt. Lett. **16**, 76 (1991).
[26] D. L. Matthews, P. L. Hagelstein, M. D. Rosen, M. J. Eckart, N. M. Ceglio, A. U. Hazi, H. Medecki, B. J. MacGowan, J. E. Trebes, B. L. Whitten, E. M. Campbell, C. W. Hatcher, A. M. Hawryluk, R. L. Kauffman, L. D. Pleasance, G. Rambach, J. H. Scofield, G. Stone, and T. A. Weaver, Phys. Rev. Lett. **54**, 110 (1985).